

## Shock properties of H<sub>2</sub>O ice

Sarah T. Stewart<sup>1</sup> and Thomas J. Ahrens

Lindhurst Laboratory of Experimental Geophysics, California Institute of Technology, Pasadena, California, USA

Received 10 June 2004; revised 28 October 2004; accepted 21 December 2004; published 18 March 2005.

[1] To understand the mechanics and thermodynamics of impacts on, and collisions between, icy planetary bodies, we measured the dynamic strength and shock states in H<sub>2</sub>O ice. Here, we expand upon previous analyses and present a complete description of the phases, temperature, entropy, and sound velocity along the ice shock Hugoniot. Derived from shock wave measurements centered at initial temperatures ( $T_0$ ) of 100 K and 263 K, the Hugoniot is composed of five regions: (1) elastic shocks in ice Ih, (2) ice Ih deformation shocks, and shock transformation to (3) ice VI, (4) ice VII, and (5) liquid water. In each region, data obtained at different initial temperatures are described by a single  $U_S - \Delta u_p$  shock equation of state. The dynamic strength of ice Ih is strongly dependent on initial temperature, and the Hugoniot Elastic Limit varies from 0.05 to 0.62 GPa, as a function of temperature and peak shock stress. We present new bulk sound velocity measurements and release profiles from shock pressures between 0.4 and 1.2 GPa. We report revised values for the shock pressures required to induce incipient melting ( $0.6 \pm 0.05$ ,  $1.6 \pm 0.3$  GPa) and complete melting ( $2.5 \pm 0.1$ ,  $4.1 \pm 0.3$  GPa) upon isentropic release from the shock state (for  $T_0 = 263$ , 100 K). On account of the >40% density increase upon transformation from ice Ih to ices VI and VII, the critical shock pressures required for melting are factors of 2 to 10 lower than earlier predicted. Consequently, hypervelocity impact cratering on planetary surfaces and mutual collisions between porous cometsimals will result in abundant shock-induced melting throughout the solar system.

**Citation:** Stewart, S. T., and T. J. Ahrens (2005), Shock properties of H<sub>2</sub>O ice, *J. Geophys. Res.*, 110, E03005, doi:10.1029/2004JE002305.

### 1. Introduction

[2] The response of rocks and minerals to shock compression governs the outcome of collisions between planetary bodies. The mechanical and thermodynamic work from an impact event may be derived from a material's shock Hugoniot, which describes the dynamic strength and possible shock-compressed states, as well as the existence and properties of high-pressure phases. The H<sub>2</sub>O ice Hugoniot is needed to model collisions onto and between the ice-rich planets and cometsimals in the outer solar system and to interpret a wide range of impact processes, including shock-induced melting and vaporization, cratering mechanics, and mass transfer via accretion, erosion, or catastrophic disruption.

[3] Previous studies of the shock Hugoniot of nonporous ice (Table 1), primarily focused on terrestrial applications and conducted around 263 K [Anderson, 1968; Gaffney, 1973; Larson *et al.*, 1973; Bakanova *et al.*, 1976; Gaffney and Ahrens, 1980; Larson, 1984; Gaffney and Smith, 1994; Davies and Smith, 1994], have had difficulty identifying the

onset of shock-induced transformations to high-pressure phases and yielded conflicting explanations of the dynamic yield mechanism [Larson, 1984; Gaffney, 1985]. Although the high-pressure region of the ice Hugoniot (>8 GPa) has been well characterized, the low-pressure region has been difficult to interpret [Gaffney, 1985]. In addition, observation of shock-induced transformation to high-pressure phases under terrestrial conditions has led to questions about the possibility and significance of impact production of ice polymorphs on planetary surfaces [Gaffney and Matson, 1980].

[4] Because ices on the surfaces of icy bodies in the outer solar system exist at temperatures much below 263 K (e.g., around 200 K on Mars to around 40 K on Pluto), we measured the shock properties of the most common low-pressure phase, ice Ih, at an initial temperature of 100 K to derive a new ice Hugoniot that is applicable throughout most of the solar system. Using previously published shock and static data [Stewart and Ahrens, 2003], we present the derivation of the complete shock Hugoniot for H<sub>2</sub>O ice and the temperature dependence of the dynamic strength of H<sub>2</sub>O ice. The original experiment data records are provided in the auxiliary material<sup>1</sup>. Here, we present new calculations for the temperature and entropy along the Hugoniot, including

<sup>1</sup>Now at Department of Earth and Planetary Sciences, Harvard University, Cambridge, Massachusetts, USA.

**Table 1.** H<sub>2</sub>O Ice Shock Data

Symbol	Source	$P_s^a$ GPa	Note <sup>b</sup>
<i>Elastic Shock Waves</i>			
■	this work	0.35–0.62	P
◇	Larson [1984] <sup>c</sup>	0.15–0.30	P
△	Larson [1984] <sup>c</sup>	0.16–0.19	S
▷	Gaffney and Smith [1994]	0.05–0.11	P
◁	Davies and Smith [1994]	0.05–0.23	P
<i>Deformation Shock Waves</i>			
★	this work	0.37–5.32	P
▽	Anderson [1968]	3.55–30.10	P
⊙	Anderson [1968]	18.00–27.40	S
⊠	Gaffney [1973]	0.46–0.85	P
□	Bakanova et al. [1976]	3.43–50.30	P
⊗	Gaffney and Ahrens [1980]	1.91	P
◆	Larson [1984] <sup>c</sup>	0.42–3.56	P
▲	Larson [1984] <sup>c</sup>	0.26–0.31	S
▶	Gaffney and Smith [1994]	0.68–2.92	P
◀	Davies and Smith [1994]	0.36–4.45	P

<sup>a</sup>Elastic shock amplitudes are principal stress; deformation shock amplitudes are pressure.

<sup>b</sup>P, polycrystalline ice sample; S, single crystal ice sample.

<sup>c</sup>Includes revised analysis of data from Larson et al. [1973].

a detailed examination of the formation and survivability of high-pressure phases. Release from the shock state is divided into three regions on the basis of sound velocity measurements and release profiles, including new measurements at shock pressures between 0.4 and 1.2 GPa. Finally, we derive revised criteria for shock-induced melting of H<sub>2</sub>O at 100 K and 263 K and discuss the implications of this work for impact cratering processes in the solar system.

## 2. Experiments and Data Analysis

### 2.1. Experiment Description

[5] Shock wave profiles in ice were directly measured using the embedded electromagnetic particle velocity gauge technique [Dremin and Shvedov, 1964; Dremin and Adadurov, 1964; Petersen et al., 1970]. Each target (Figure 1), composed of three or four gauges centered between ice discs held together by a polycarbonate frame, was hung in the presence of a magnetic field perpendicular to the long axis of the 40-mm single stage propellant gun in the Lindhurst Laboratory of Experimental Geophysics. When subject to an impact, the particle motion from the shock wave induces a voltage,  $E$ , across the gauges, given by

$$E(t) = HLu_p(t), \quad (1)$$

which was recorded by 500 MHz digital storage oscilloscopes. Here,  $H$  is the magnetic field strength in Tesla,  $L$  is the gauge length (0.009 m), and  $u_p(t)$  is the Lagrangian particle velocity in m s<sup>-1</sup> as a function of time  $t$ .

[6] Ice targets were prepared in the Caltech Cold Laboratory at or below  $-8^\circ\text{C}$ . The particle velocity gauges (Dynasen Inc., Goleta, CA) were composed of a loop of 0.5-mil (12.7- $\mu\text{m}$ ) thick copper film (9 mm length, 4 mm width, and 0.5 mm wide leads) between two 1-mil layers of polyimide. The ice discs were typically 3 mm thick, 50 mm in diameter, and cored perpendicular to the ice  $h$ -axis from a block of transparent solid ice (Carving Ice, Anaheim, CA). Each disc was polished parallel within 0.1 mm. In most experiments, a gauge was placed on the

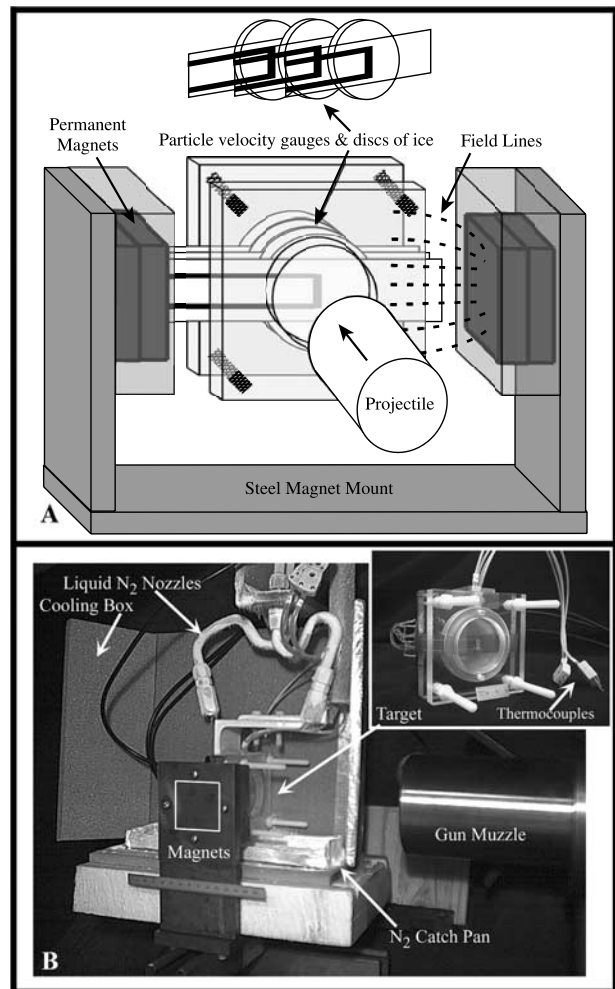


**Figure 1.** (a) Experiment schematic for particle velocity gauge technique [from Stewart and Ahrens, 2003]. Electromagnetic particle velocity gauges are embedded between ice discs. Motion due to impact is perpendicular to magnetic field lines. (b) Target is cooled with liquid nitrogen spray prior to impact.

face of the first ice disc and held in place by a 0.7-mm thick polycarbonate disc, which formed the impact surface. On the basis of the longitudinal sound speed in polyimide (2.72 km s<sup>-1</sup> [Marsh, 1980]), the 2.5-mil (63.5-μm) thick gauges equilibrate with the surrounding ice within about 20 ns, an order of magnitude longer than the time resolution of the oscilloscopes. Hence the resolution of the shock profile is limited by the gauge thickness. Because the rise times of the measured shock fronts were greater than 20 ns, the gauges reacted minimally with the ice shock, avoiding experimental difficulties related to impedance mismatch between the gauge and ice encountered in previous work [e.g., Gaffney, 1973; Gaffney and Smith, 1994; Davies and Smith, 1994].

[7] The target was hung such that the gauges embedded within the ice sample remained within a 2 × 2 × 2 cm volume, nearly uniform magnetic field, for the duration of the experiment. The field was produced by four 0.122 Tesla NdFeB permanent magnets (size 2 × 2 × 1/2 in., Magnet Sales & Mfg. Inc., Culver City, CA), assembled in pairs within a U-shaped steel mount (Figure 1). The target and magnetic field are aligned perpendicular to the barrel axis by reflecting the light from a barrel-aligned laser back to the source, over a 20 m path, producing an alignment within 1 milliradians. Before each experiment, the magnetic field strength was measured using a transverse Hall probe (Magnetic Instrumentation Inc.). The field variation and the scatter in the field measurements, both typically <0.5 milliTesla, resulted in less than a 1% uncertainty in particle velocity.

[8] The target was cooled by liquid nitrogen spray within a thermally insulating enclosure (1.27-cm thick PVC foam). Because the ice was not confined by the target assembly, it did not fracture upon cooling. Ice temperature was measured with two embedded Omega chromel-alumel thermocouples. Once the ice was cooled to 100 K or below, the target tank was evacuated to pressures between 25 and 55 Pa prior to impact. The target temperature for each experiment, in the range 90–100 K, is included in the auxiliary material.

[9] The velocity of the polycarbonate projectiles (40-mm diameter cylinders, normally >40 mm long) were measured within 1% by the time interval between extinction of three He-Ne laser beams in the projectile path and from a double X-ray exposure of the projectile at a measured time separation [cf. Miller *et al.*, 1991].

## 2.2. Lagrangian Data Analysis

[10] Lagrangian analysis of the gauge records yields the shock loading and unloading stress-volume paths when the conditions of uniaxial strain are satisfied [Cowperthwaite and Williams, 1971; Fowles and Williams, 1970]. The voltage record was converted to particle velocity by equation (1) and the measured magnitude of the magnetic field. On the basis of conservation of mass and linear momentum,

$$\left(\frac{\partial V}{\partial u_p}\right)_h = -\frac{V_0}{C_{u_p}}, \quad (2a)$$

$$\left(\frac{\partial \sigma}{\partial u_p}\right)_h = \frac{C_\sigma}{V_0}, \quad (2b)$$

where  $V$  is the specific volume,  $V_0$  is the initial specific volume,  $h$  is the Lagrangian coordinate corresponding to the initial position of the gauge, and  $\sigma$  is the principal stress under one-dimensional strain. In a steady shock wave, the phase velocities,  $C_{u_p}$  and  $C_\sigma$ , are equal ( $C_{u_p} = C_\sigma$ ), where

$$C_{u_p} = (\partial h / \partial t)_{u_p}, \quad (3a)$$

$$C_\sigma = (\partial h / \partial t)_\sigma. \quad (3b)$$

Because shock fronts in ice have multiple-wave structures, however, the phase velocities are not independent of stress [Larson, 1984].

[11] The rise time of the wave at the impact plane is non-zero, so the phase velocity is calculated as a continuous function of  $u_p$  using the Lagrangian distance,  $h_g$ , and travel time,  $\Delta t(u_p)_g$ , from the impact plane to each embedded gauge,  $g$ . At each gauge, the phase velocity,  $C(u_p)$ , is given by  $h_g / \Delta t(u_p)_g$ . Now equations (2a) and (2b) may be integrated to calculate the stress and specific volume as a function of time for each embedded gauge, as shown in Figure 2. The initial specific volume,  $V_0$ , is taken from the crystal density of ice at the initial temperature [Hobbs, 1974], and the initial pressure is considered negligible.

[12] For each wave in the shock front, subscripted  $i$ , the Lagrangian shock velocity,  $U_{S,i}^L$ , is equal to the phase velocity in that wave front,  $C(u_p)_i$ . In Lagrangian coordinates, each wave in the shock front travels the same distance,  $h_g$ . In Eulerian coordinates (the lab frame of reference), the second (and third) wave travels through a pre-compressed medium such that the Eulerian wave velocity is reduced by the compression ratio,  $U_{S,i} = (V_i/V_0)U_{S,i}^L$ , where  $V_i$  is the specific volume of shock state in the  $i$ th wave and  $V_0$  is the initial specific volume. Similarly, the second and third wave travels through a material in motion, and the Lagrangian wave velocity is larger than the Eulerian wave velocity by the particle velocity in the previous wave,  $_{i-1}$ , such that  $U_{S,i}^L = U_{S,i} + u_{p,i-1}$  (Figure 2b). We calculate the Eulerian shock velocity and increase in particle velocity for each wave in the shock front (e.g., Figure 2a).

[13] For each shock state, the peak particle velocity, stress, and compressed volume is determined by averaging the top of the wave profile (via equations (2a) and (2b)) and the Eulerian velocity is determined by the time of arrival of the foot of the wave. In some cases, the particle velocity at the peak of the intermediate wave continues to rise slowly until the arrival of the main shock and peak values for the precursor state are averaged over this time period. The results are given in Table 2. The tabulated error associated with each measurement is the larger of the scatter in the top of the wave or the formal error propagated throughout the Lagrangian analysis [Bevington and Robinson, 1992]. The measured final state particle velocities were within 2% of the standard impedance-match solution [Ahrens, 1987] derived from the polycarbonate Hugoniot [Marsh, 1980]. Wave profiles and integrated stress-volume paths from each experiment are included in the online auxiliary materials.<sup>1</sup>

[14] For each wave in the shock front, the initial state, subscripted  $_0$ , and final state, subscripted  $_i$ , are related

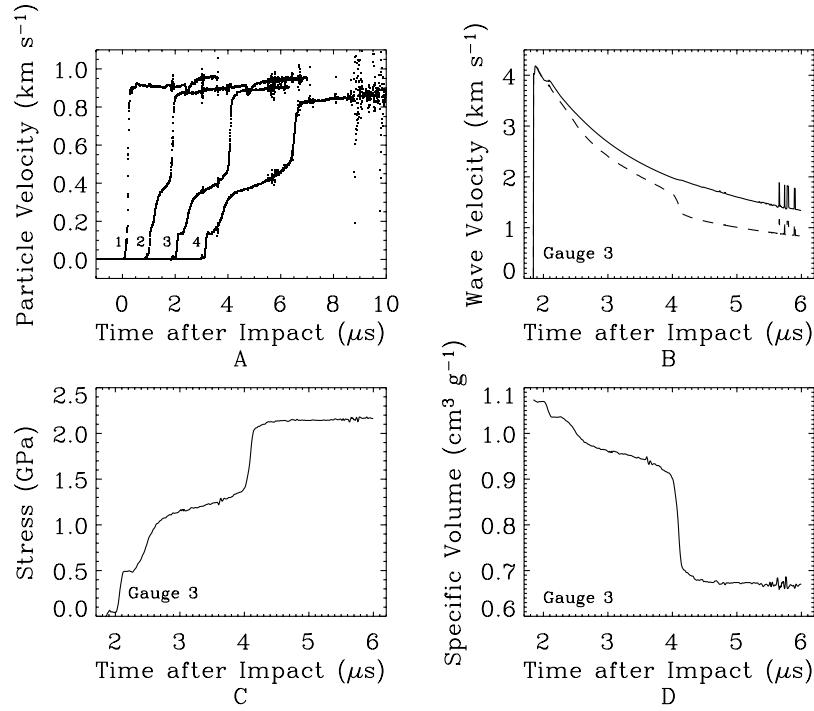


**Figure 2.** Lagrangian analysis method. (a) Particle velocity traces for all 4 gauges in shot 1043. (b) Lagrangian wave velocity (solid line) and Eulerian wave velocity (dashed line) versus time between gauges 1 and 3 (located at  $h = 7.50$  mm). (c) Stress versus time from equation (2b). (d) Volume versus time from equation (2a).

through the Rankine-Hugoniot (RH) mass, momentum and energy conservation equations [Rice *et al.*, 1958],

$$u_{p,i} - u_{p,0} = U_S \left( 1 - \frac{V_i}{V_0} \right), \quad (4a)$$

$$P_i - P_0 = \frac{U_S}{V_0} (u_{p,i} - u_{p,0}), \quad (4b)$$

$$E_i - E_0 = \frac{1}{2} (P_i + P_0) (V_0 - V_i), \quad (4c)$$

where  $u_p$  is the particle velocity,  $U_S$  is the Eulerian shock wave velocity,  $P$  is pressure, and  $E$  is the specific internal energy. The tabulated Eulerian shock wave velocity,  $U_S$ , a material property and independent of the motion of the material, is used in the derivation of the Hugoniot.

### 3. Results and Interpretation

#### 3.1. $U_S - \Delta u_p$ Shock Equation of State

[15] The dynamic response of ice Ih is temperature dependent, and multiple-wave shock fronts, which include phase transformation shocks, develop when the peak pressure is less than  $\sim 6$  GPa. Above  $\sim 6$  GPa, shocks in ice propagate as a single wave shock front. To separate the effects of temperature and phase transformations, we consider each wave independently. Figure 3 compares two idealized multiple-wave shock profiles and their corresponding stress-volume loading paths, based on this

work and Larson [1984], at different initial temperatures with peak shock stress near 1.6 GPa. The final wave in both shock fronts is a transformation shock to the ice VI structure (see section 3.7.1), but the amplitude of the leading elastic shock,  $\sigma_E$ , is much larger at  $T_0 = 100$  K, with  $\sigma_E = 0.55$  GPa (shot 1047, gauge 2), than at 263 K, when  $\sigma_E = 0.17$  GPa (Larson experiment with 1.62 GPa peak shock state). In addition, a steady 3-wave shock front develops at 100 K, with an intermediate shock in the ice Ih structure, but there is no intermediate shock in the 263 K data. Although the final particle velocity,  $\Sigma u_p$ , and stress are similar in these two experiments, the loading path and shock front depend significantly on the initial temperature.

[16] Previously,  $U_S - \Sigma u_p$  data from different studies were combined to derive the shock Hugoniot [e.g., Gaffney, 1985], but the temperature and rate dependent response of ice Ih complicates direct comparison of  $\Sigma u_p$  with the new data. A rigorous comparison between data sets is made by considering  $U_S$  and  $\Delta u_p$  for each wave in the shock front. In this manner, each wave is described by the RH equations (equation (4)) centered in the previous state. For the  $T_0 = 100$  K data in Figure 3, the ice VI transformation shock to the final shock state is centered in the ice Ih shock state; however, for  $T_0 = 263$  K, the ice VI shock to the final state is centered in the elastic shock state.

[17] The new data are combined with previous data to derive the shock Hugoniot, for pressures up to 51 GPa. In the multiple-wave region  $< 6$  GPa, we include only data that (1) resolve each wave in the shock front to account for the variations in the magnitude of the elastic precursor wave and (2) record steady shock waves in order to derive



**Table 2.** One Hundred Kelvin Ice Hugoniot Data

Exp.	Shock Feature <sup>a</sup>	$u_p$ , m s <sup>-1</sup>	$U_s$ , m s <sup>-1</sup>	$\rho$ , kg m <sup>-3</sup>	$P$ , GPa and MPa
I44 <sup>b</sup>	I.P.	127.6 (5.7)	...	...	...
	Avg., 1	100.7 (0.6)	3868 (29)	958 (1.0)	0.357 (28)
	G 2, 1	105.2 (0.9)	3767 (48)	960 (1.8)	0.367 (55)
	G 2, 2 <sup>c</sup>	124.8 (3.3)	2369 (20)	970 (3.7)	0.401 (55)
	G 3, 1	96.3 (0.9)	3969 (32)	956 (0.9)	0.347 (11)
	G 3, 2 <sup>c</sup>	118.5 (2.9)	2920 (24)	965 (1.6)	0.401 (11)
	G 4, 1 <sup>c</sup>	78.2 (0.9)	4146 (38)	951 (0.9)	0.289 (11)
	G 4, 2 <sup>c</sup>	102.5 (1.6)	3125 (25)	959 (0.9)	0.359 (11)
I45	I.P.	154.9 (5.0)	...	...	...
	Avg., 1	115.3 (1.4)	3408 (25)	963 (1.0)	0.380 (7)
	G 2, 1	115.3 (1.4)	3408 (25)	963 (1.0)	0.380 (7)
	G 2, 2 <sup>c</sup>	151.3 (3.2)	2098 (60)	981 (1.4)	0.453 (7)
	G 3, 1 <sup>c</sup>	75.8 (0.7)	3591 (29)	952 (6.2)	0.255 (72)
	G 3, 2 <sup>c</sup>	135.7 (0.7)	2580 (240)	974 (6.5)	0.407 (72)
	G 4, 1 <sup>c</sup>	91.9 (1.4)	3230 (23)	959 (2.0)	0.276 (20)
	G 4, 2 <sup>c</sup>	131.5 (0.9)	2477 (76)	975 (2.1)	0.369 (20)
1046	I.P.	365.8 (2.6)	...	...	...
	Avg., 1	114.4 (1.7)	3828 (21)	961 (0.7)	0.408 (7)
	Avg., 2	267.4 (1.0)	2991 (17)	1011 (0.8)	0.860 (7)
	G 2, 1	120.9 (2.3)	3827 (30)	962 (1.0)	0.431 (9)
	G 2, 2	276.2 (1.6)	3014 (24)	1015 (1.1)	0.886 (9)
	G 3, 1	107.9 (2.5)	3830 (30)	959 (1.0)	0.384 (10)
	G 3, 2	258.5 (1.2)	2968 (23)	1008 (1.1)	0.834 (11)
1047	I.P.	701.0 (2.7)	...	...	...
	Avg., 1	155.1 (1.9)	3653 (30)	973 (6.6)	0.530 (96)
	Avg., 2	370.9 (2.0)	3219 (30)	1051 (7.7)	1.148 (96)
	Avg., 3	695.9 (8.6)	1196 (22)	1449 (20.0)	1.550 (130)
	G 2, 1	164.2 (2.7)	3597 (43)	977 (9.0)	0.550 (130)
	G 2, 2	378.7 (2.7)	3188 (39)	1057 (11.0)	1.150 (130)
	G 2, 3	695.9 (8.6)	1196 (22)	1449 (20.0)	1.550 (130)
	G 3, 1	146.1 (2.7)	3708 (42)	969 (9.4)	0.510 (140)
	G 3, 2	363.2 (3.0)	3251 (46)	1046 (11.0)	1.150 (140)
1043	I.P.	911.2 (4.8)	...	...	...
	Avg., 1	145.6 (2.2)	3855 (17)	968 (2.2)	0.525 (32)
	Avg., 2	359.4 (1.9)	3361 (15)	1041 (2.5)	1.163 (32)
	Avg., 3	882.7 (4.2)	1757 (10)	1475 (7.8)	2.131 (48)
	G 2, 1	166.5 (4.8)	3754 (29)	975 (1.7)	0.589 (23)
	G 2, 2	356.1 (3.3)	3330 (26)	1041 (2.0)	1.142 (23)
	G 2, 3	873.6 (4.5)	1811 (14)	1462 (6.4)	2.114 (23)
	G 3, 1	134.6 (3.3)	3900 (30)	965 (6.2)	0.491 (92)
	G 3, 2	359.4 (3.3)	3361 (27)	1041 (7.2)	1.160 (92)
	G 3, 3	891.9 (7.1)	1703 (15)	1489 (15.0)	2.148 (92)
	G 4, 1	135.6 (3.3)	3911 (29)	965 (1.6)	0.496 (20)
	G 4, 2	362.7 (3.3)	3391 (26)	1041 (1.8)	1.186 (20)
	G 4, 3 <sup>c</sup>	833.0 (11.0)	1604 (12)	1422 (14.0)	2.051 (20)
1045	I.P.	1606.0 (16.0)	...	...	...
	Avg., 1	157.9 (4.8)	3700 (46)	972 (7.6)	0.560 (93)
	Avg., 2	1597.0 (11.0)	3275 (34)	1727 (24.0)	5.178 (93)
	G 2, 1 <sup>c</sup>	112.2 (7.8)	3500 (1000)	960 (300.0)	0.400 (3000)
	G 2, 2 <sup>c</sup>	1581.0 (6.9)	3130 (950)	1690 (920.0)	5.100 (3000)
	G 3, 1	171.7 (6.8)	3619 (35)	976 (8.1)	0.605 (92)
	G 3, 2	1588.0 (18.0)	3235 (50)	1716 (25.0)	5.154 (92)
	G 4, 1	144.0 (6.8)	3781 (85)	969 (13.0)	0.520 (160)
	G 4, 2	1607.0 (13.0)	3315 (46)	1739 (42.0)	5.200 (160)

<sup>a</sup>Impact plane (I.P.) entry records peak particle velocity at ice-polycarbonate buffer interface. G #, # denotes gauge, numbered 1, 2, etc., from impact plane and wave number in shock front, respectively. Average values recommended for denoted wave feature by combining all reliable gauge records.

<sup>b</sup>Initial temperature 69 K.

<sup>c</sup>Indicates that this datum should be considered unreliable (usually shock front is partially attenuated). Refer to auxiliary material for each shot.

Hugoniot states. Hence data were not included from experiments that recorded only the first shock arrival [Anderson, 1968; Bakanova *et al.*, 1976; Gaffney and Ahrens, 1980] or recorded unsupported shock waves, where the peak shock stress decayed between gauges [Gaffney, 1973; Larson *et al.*, 1973; Larson, 1984; Gaffney and Smith, 1994; Davies and Smith, 1994]. We include all published data >6 GPa. Data symbols, corresponding to the source study, are defined in Table 1.

[18] By combining 100 K (low-temperature) and 263 K (temperate)  $U_s - \Delta u_p$  data, we define five regions on the ice Hugoniot that correspond to different shock processes (Figure 4): (1) elastic shocks, (2) deformation shocks in the initial ice Ih structure, and transformation shocks to (3) ice VI, (4) ice VII and (5) liquid water Stewart and Ahrens [2003]. The coefficients for the shock equation of state (EOS), least squares linear fits to each segment, are given in Table 3. Linear  $U_s - \Delta u_p$  fits are justified by the negligible

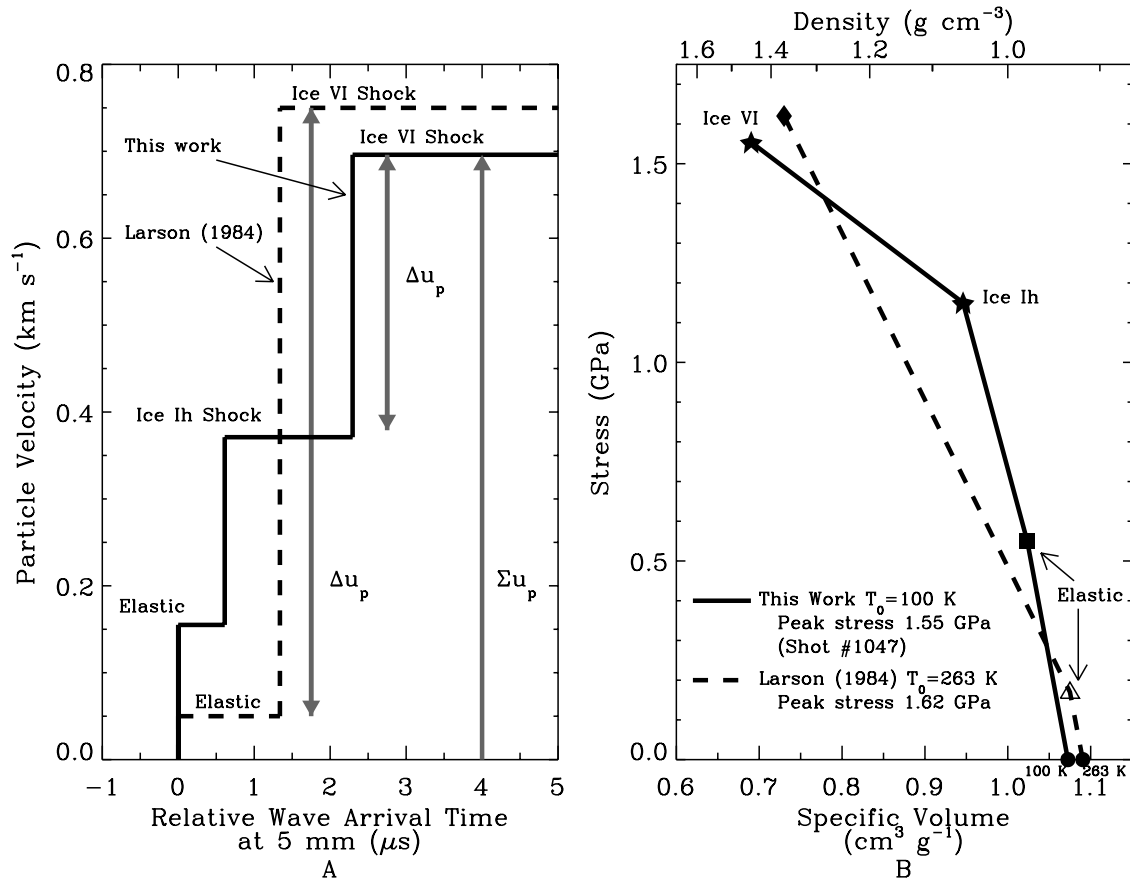


**Figure 3.** Idealized ~1.6 GPa shock profiles in solid ice comparing this work ( $T_0 = 100$  K, solid lines) to Larson [1984] ( $T_0 = 263$  K, dashed lines). (a) Multiple-wave shock front profiles 5 mm from impact plane. Full compression is achieved by two or three discrete shock jumps. (b) Compression curves corresponding to shock profiles in Figure 3a.

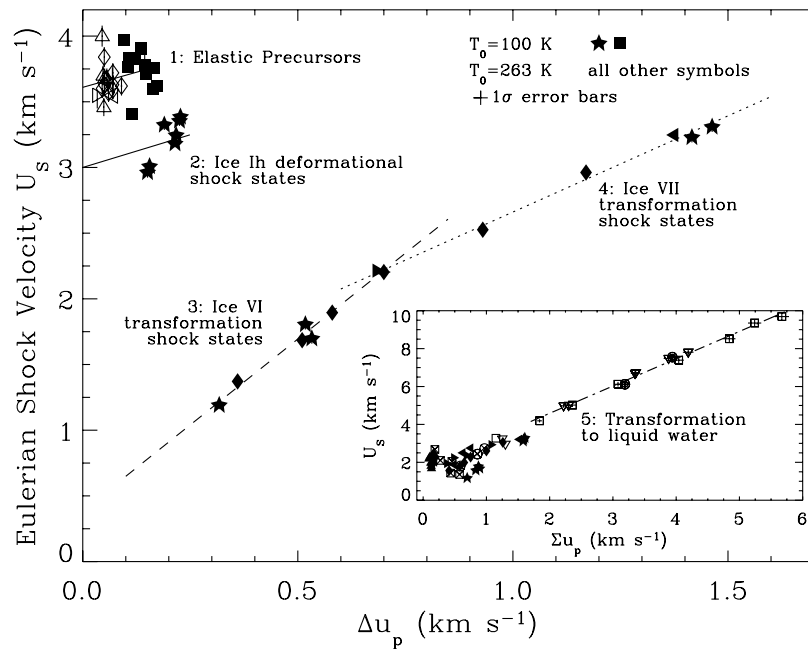


**Figure 4.** H<sub>2</sub>O ice  $U_s - \Delta u_p$  shock equation of state divided into five regions: (1) elastic shocks, (2) deformation shocks in ice Ih, and transformation shocks to (3) ice VI, (4) ice VII, and (5) liquid water [from Stewart and Ahrens, 2003]. Symbols correspond to different data sources (Table 1); inset shows all previous ice data.

**Table 3.**  $U_S - \Delta u_p$  Shock Equation of State,  $U_S = c + s\Delta u_p$ , Used to Calculate Solid Ice Hugoniot<sup>a</sup>

Hugoniot Region	c, m s <sup>-1</sup>	s, ...	$\Delta u_p$ Range, m s <sup>-1</sup>	
			min	max
1. Elastic	3610 (±61)	0.92 (±.63)	0	175
2. Ice Ih <sup>b</sup>	3000 (...)	1.00 (±.80)	0	230
3. Ice VI	388 (±78)	2.61 (±.14)	100	850
4. Ice VII	1200 (±140)	1.46 (±.11)	600	1540
5. Liquid	1700 (±130)	1.440 (±.035)	1590	...

<sup>a</sup>After Stewart and Ahrens [2003]. 1 $\sigma$  uncertainties given in parentheses.

<sup>b</sup>Steady shock waves do not develop unless overdriven at low temperatures. Fixed bulk sound speed for ice Ih.

effect of the second derivative of the bulk modulus over this pressure range [Ruoff, 1967; Jeanloz, 1979].

[19] The response of ice Ih to shock is strongly dependent on the initial temperature. First, the mean amplitude of all the elastic shocks (region 1) in low-temperature ice ( $0.47 \pm 0.09$  GPa) is 2.5 times larger than in temperate ice ( $0.19 \pm 0.05$  GPa). Second, in low-temperature ice, steady ice Ih deformation shocks (region 2) develop as an intermediate state in the shock front between the elastic wave and the transformation wave to ice VI (e.g., Figure 3). In temperate ice, however, no intermediate steady ice Ih shocks were observed, and Larson [1984] reported two-wave shock fronts in all 263 K experiments, with peak shock stress spanning 0.26–3.56 GPa.

[20] The  $U_S - \Delta u_p$  EOS for shock-induced solid-solid phase transformations (regions 3 and 4), however, are independent of initial temperature over the range 100–263 K. By considering  $\Delta u_p$  instead of  $\Sigma u_p$ , the temperature dependent response of the initial ice Ih phase is removed from these regions of the shock EOS. At pressures above 6 GPa ( $\Sigma u_p \geq 1590$  m s<sup>-1</sup>, region 5), the shock velocities are greater than the longitudinal wave speed,

and the elastic precursor is overdriven, forming a single-wave shock front.

[21] For comparison to the new  $U_S - \Delta u_p$  EOS, all the published ice Hugoniot data are plotted as  $U_S - \Sigma u_p$  in the Figure 4 inset (elastic shocks are omitted). Note the considerable scatter in the <6 GPa data ( $\Sigma u_p < 1590$  m s<sup>-1</sup>) compared to the >6 GPa data. We attribute the scatter to the inclusion of decaying shock waves and variation in the amplitude of the elastic shock precursor. In the range  $150 < \Sigma u_p < 2000$  m s<sup>-1</sup> (inset, regions 3 and 4), the shock velocities in the 100 K data (★) are systematically slower than the 263 K data because the large-amplitude elastic shocks and intermediate ice Ih shocks reduce the amplitude (and the corresponding shock velocity) of the final phase transformation shock wave compared to the temperate ice data.

### 3.2. $P - V$ Hugoniot

[22] The shock data may be transformed from  $U_S - \Delta u_p$  to stress-volume ( $\sigma - V$ ) using the RH equations (equation (4)). In Figure 5, the 100 K (solid line) and 263 K (dashed line) Hugoniots are constructed in segments

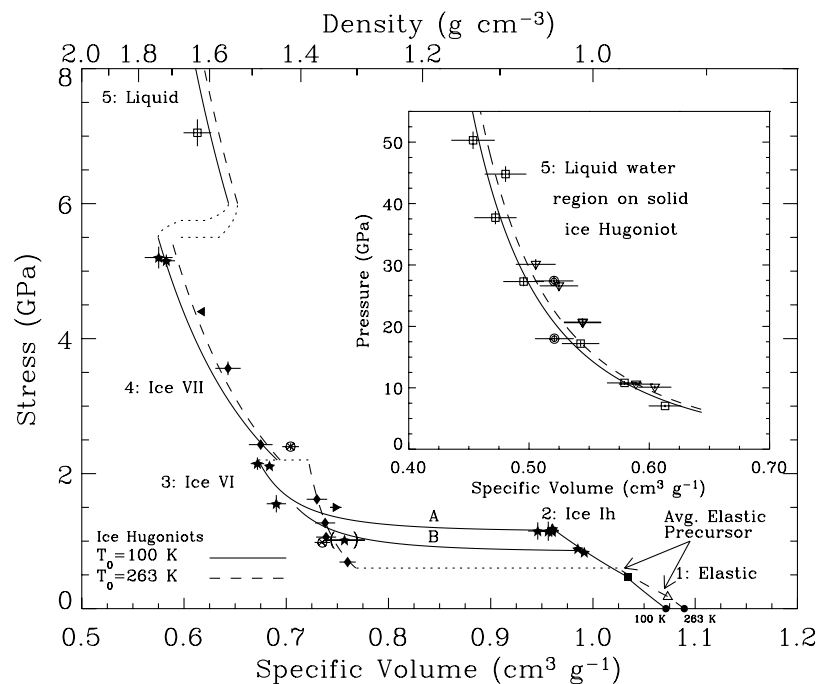


**Figure 5.** H<sub>2</sub>O ice Hugoniots centered at  $T_0 = 100$  (solid lines) and 263 K (dashed lines) [from Stewart and Ahrens, 2003]. Dotted lines connect Hugoniot segments derived from  $U_S - \Delta u_p$  shock equation of state (Table 3). Two possible loci (A and B) are shown on the 100 K Hugoniot.

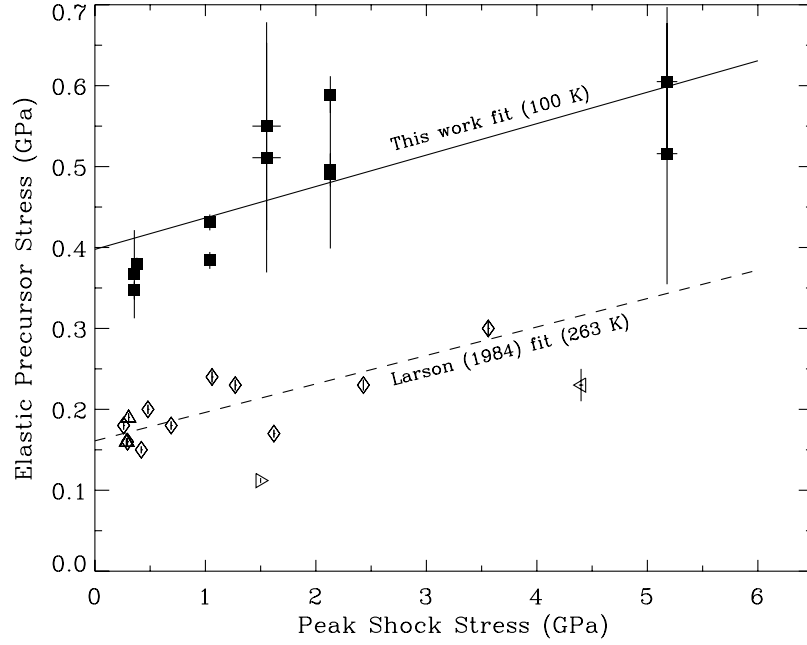


**Figure 6.** Model for peak shock stress-temperature dependence of elastic shock precursor amplitude (equation (5)).

corresponding to each type of shock wave: elastic shock, ice Ih shock, and transformation shocks to ice VI, VII, and liquid. The Hugoniot is centered  $V_0 = 1.089$  and  $1.073 \text{ cm}^3 \text{ g}^{-1}$  at 263 and 100 K, respectively [Hobbs, 1974; Röttger *et al.*, 1994]. The locus of elastic shocks, region 1, is calculated using the elastic  $U_S - \Delta u_p$  EOS (Table 3) and  $V_0$ .

[23] On the 100 K Hugoniot, the next region, ice Ih deformation shocks, is obtained with the ice Ih  $U_S - \Delta u_p$  EOS using the 100 K mean elastic precursor shock ( $1.03 \text{ cm}^3 \text{ g}^{-1}$  and 0.47 GPa, ■ in Figure 5) as the initial state. The maximum ice Ih shock has an amplitude of 1.16 GPa. Impact stresses reaching the next region, ice VI, produce three-wave shock fronts, and in our experiments, the amplitude of the intermediate ice Ih shock varies with the peak shock stress (see section 3.7.1). Hence the initial state for the ice VI region is variable (shown as the segments labeled A and B in Figure 5). The ice VII region begins above 2.2 GPa, where the mean elastic precursor is used as the initial state, forming two-wave shock fronts.

[24] At low temperatures, steady ice Ih deformation shocks develop only as part of three-wave shock fronts. At both initial temperatures, impacts resulting in peak stresses below 0.6 GPa drives a shock that separates into a two-wave profile, composed of the elastic precursor and a decaying plastic wave (not plotted). Note that there are no 263 K steady shock data points in the ice Ih region of Figures 4 and 5.

[25] On the 263 K Hugoniot, the ice VI region begins at 0.6 GPa and the ice VII region begins above 2.2 GPa. Both segments use the 263 K mean elastic precursor ( $1.07 \text{ cm}^3 \text{ g}^{-1}$ , 0.18 GPa, in Figure 5), as the initial state for application of the  $U_S - \Delta u_p$  EOS. Note that the same  $U_S - \Delta u_p$  EOS (Table 3) is used to calculate the ice VI region on both the 100 K and 263 K Hugoniot in Figure 5. The offset between the Hugoniot in this region arises from the different initial state used in application of equation (4).

[26] On both the low-temperature and temperate Hugoniot, shocks to the liquid water region ( $\geq 6$  GPa) overdrive the elastic shock precursor. This region on the Hugoniot (Figure 5, inset) is calculated with the liquid water  $U_S - \Delta u_p$  EOS using the zero-pressure volume as the initial state (off scale of inset). The experimental technique used in this study did not reach shock pressures above 6 GPa, and no other low-temperature data in this pressure range are available. The 100 K Hugoniot is derived assuming that the liquid water  $U_S - \Delta u_p$  EOS is independent of initial temperature, as is the case in the ice VI and VII segments.

### 3.3. Elastic Shock Precursors

[27] We find that the amplitude of the elastic shock stress is very sensitive to the initial temperature, as seen in the offset in  $\Delta u_p$  between the low-temperature (■) and temperate (open symbols) data in Figure 4. The amplitude of the elastic shock in ice at  $T_0 \sim 263$  K lies between 0.05 and 0.30 GPa, whereas the elastic shocks in  $T_0 \sim 100$  K ice reach values between 0.35 and 0.61 GPa (Table 1). Although commonly referred to as the Hugoniot Elastic Limit (HEL), implying a single value, the amplitude of the elastic shock wave in ice varies by a factor of six in the available data.

[28] In addition to temperature, the elastic shock amplitude is also correlated with the peak shock pressure, as previously observed by Larson [1984]. In Figure 6, the dependence of the elastic precursor amplitude  $\sigma_E$  on the peak shock stress  $\sigma_S$  is fit by linear segments:

$$\sigma_E = \begin{cases} 0.398 (\pm 0.029) + 0.039 (\pm 0.012) \sigma_S, & \text{at } T \sim 100 \text{ K} \\ 0.161 (\pm 0.010) + 0.035 (\pm 0.007) \sigma_S, & \text{at } T \sim 263 \text{ K.} \end{cases} \quad (5)$$

Linear fits provide a good approximation of the peak shock stress dependence, although there is some indication,



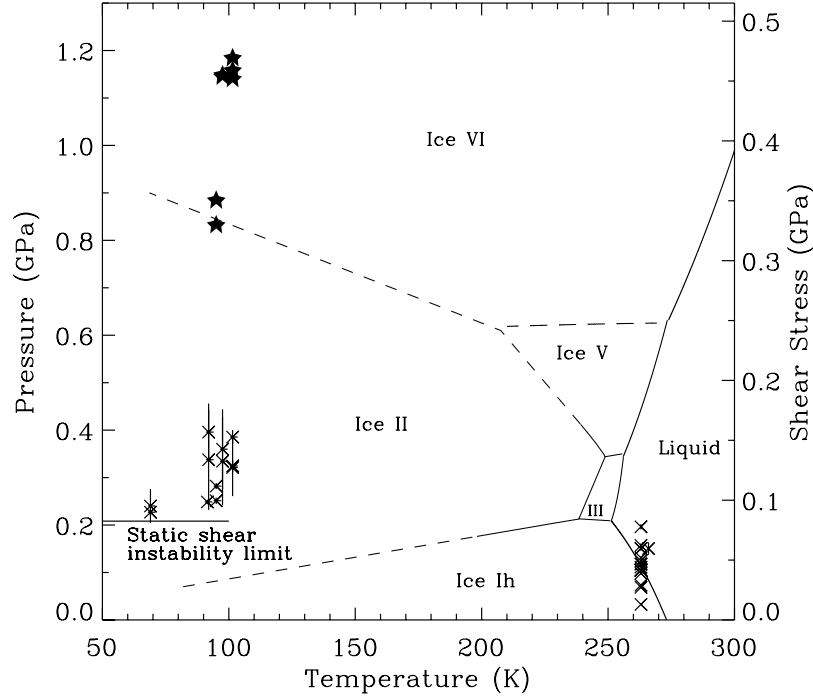


**Figure 7.** One hundred Kelvin ice Ih deformation shock stress (★) on  $P - T$  phase diagram with 100 K (this work) and 263 K [Larson, 1984] elastic shock precursor states, ×, reduced to hydrostatic pressure (left axis) and shear stress (right axis). All data plotted against initial temperature.

especially in the low-temperature data, that the amplitude of the elastic precursor approaches a limit of  $0.53 \pm 0.05$  GPa for  $T_0 \sim 100$  K and only  $0.25 \pm 0.04$  GPa for  $T_0 \sim 263$  K. A similar peak shock pressure correlation is observed in SiO<sub>2</sub>, where the elastic precursor amplitude is also dependent on the crystal orientation [Fowles, 1967]. However, Larson [1984] did not observe any dependence of the elastic precursor or the final shock state on the crystal axis orientation. Therefore we infer that the ice Ih HEL is much more sensitive to temperature than crystal orientation.

[29] The elastic shock wave propagates at the longitudinal sound speed,  $c_l$ . As Larson [1984] did not detect changes in sound speed at different crystal orientations, we use isotropic values for the elastic moduli. The temperature (at zero pressure) and pressure dependence (at 237.5 K) of the elastic constants were measured by Gagnon *et al.* [1988] and averaged for isotropic ice [Voigt, 1928; Simmons and Wang, 1971]. In the 100 K experiments, elastic precursor wave velocities are systematically lower than ideal isotropic ice by about  $0.2 \text{ km s}^{-1}$ , with an average wave velocity of  $3.65 \pm 0.14 \text{ km s}^{-1}$  at 263 K and  $3.76 \pm 0.16 \text{ km s}^{-1}$  at 100 K. We speculate that the offset may be a result of imperfections in the preparation of the ice samples, such as trace porosity (e.g., bubbles or cracks). Furthermore, the elastic wave velocities measured in samples prepared within a given study have a wide range of scatter, attesting to the difficulty in making identical ice samples.

[30] The dynamic yield strength (under uniaxial strain) is about  $10^2$  times the static compressive strength (under uniaxial stress) [e.g., Hawkes and Mellor, 1972]. Increasing compressive and tensile strength with increasing strain rate is well established [Hawkes and Mellor, 1972; Lange and Ahrens, 1983; Stewart and Ahrens, 1999], and the strain

rates in the shock experiments, at  $10^3 - 10^4 \text{ s}^{-1}$ , are much higher than the static experiments, at  $10^{-7} - 10^{-4} \text{ s}^{-1}$ . As a result, the elastic shock states fall significantly outside the equilibrium stability field of ice Ih, shown in Figure 7.

[31] Both the static and dynamic strength are strongly dependent on temperature and strain rate [e.g., Durham *et al.*, 1998; Durham and Stern, 2001]. Under shock, the peak stress (Figure 6) is a proxy for strain rate [Sweogle and Grady, 1985]. Hence, for shock pressures just above the dynamic yield stress (up to about 2 GPa), the dynamic strength of ice has a noticeable dependence on strain rate, and with increasing shock pressure, the yield strength seems to reach a plateau determined by the dynamic yield limit for the initial temperature. More data are needed to clarify the dependence of dynamic strength on temperature and strain rate.

[32] In Figure 7, the elastic shock stress,  $\sigma_1$ , has been reduced to pressure,  $P$ , by

$$P = \frac{(\sigma_1 + 2\sigma_2)}{3} = \frac{1}{3} \left( \frac{1 + \nu}{1 - \nu} \right) \sigma_1, \quad (6)$$

where the perpendicular stresses are  $\sigma_2 = \sigma_3 = \nu\sigma_1/(1 - \nu)$  under uniaxial strain, and  $\nu = 0.325$  is Poisson's ratio in ice Ih [Petrenko and Whitworth, 1999] (the small dependence of  $\nu$  on temperature is neglected). Because elastic shock compression is essentially isothermal, the pressure of the elastic shock states (×) are plotted against the initial temperature in Figure 7.

[33] By comparing the elastic shock stress to the static phase diagram, Larson [1984] suggested that the maximum amplitude was controlled by the onset of melting; however, more recent work has shown that brittle failure is more

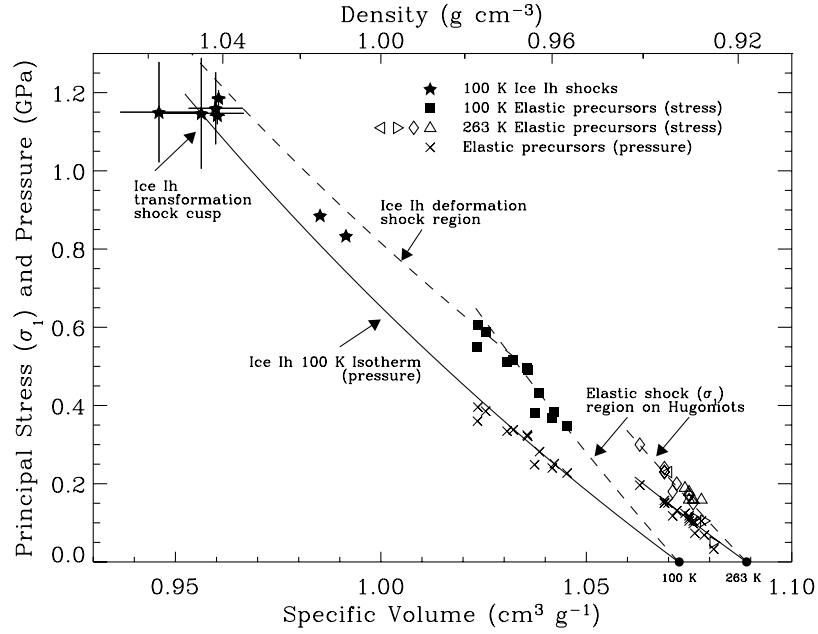


**Figure 8.** Elastic and ice Ih deformation shock regions on ice Hugoniot (dashed lines). The 100 K ice Ih deformation shocks have a limiting value of 1.16 GPa, forming a cusp on the Hugoniot. Principal stress on Hugoniot approaches extrapolated 100 K isotherm (solid line), indicating loss of strength along Hugoniot and little shock heating. Pressures in elastic shock states (×) lie on isothermal compression curves.

likely. *Gaffney* [1985] argued that the energy deposited in elastic shocks is insufficient to initialize melting (see his Figure 9), and *Arakawa et al.* [2000] directly imaged a brittle failure wave generated by a decaying shock wave (from about 10 GPa to 0.03 GPa) in a solid ice block at 263 K. *Arakawa et al.* [2000] also recovered an ice sample shocked to just above the HEL (0.3 GPa) and observed dense shear cracks spaced at 100's  $\mu\text{m}$ . The interpretation that brittle failure controls the maximum elastic shock stress is supported by both the strength dependance on temperature and strain rate and the location of the HEL states in the ice phase diagram.

[34] The mechanism for brittle failure in a shock may be related to transformational faulting in the shear bands. *Durham et al.* [1983, 1998] found that, under confined conditions at 77 K, ice Ih fails from stress interactions with microinclusions of ice II and that the maximum differential stress at failure is nearly constant at 0.165 GPa above confining pressures of 50 MPa. Materials subject to shock support shear stress until failure at the HEL. The shear stress,  $\tau$ , is given by  $\tau = (\sigma_1 - \sigma_2)/2$ , where  $\tau = 0.26\sigma_1$  in ice under uniaxial strain. The elastic precursor amplitude appears to approach a limiting value with increasing shock stress (Figure 6), where the limiting shear stress under shock ( $\tau = 0.26 \max(\sigma_E) = 0.14$  GPa, Figure 7, right vertical axis) is larger than in static experiments (0.0825 GPa [*Durham et al.*, 1998]) because of the higher strain rate. At 263 K, the brittle failure mechanism may also be transformational faulting, with liquid water microinclusions in shear zones rather than ice II, as suggested by *Kato et al.* [2001].

[35] Next, we compare the elastic shock data to the principal isotherm, derived from the shock EOS, extended beyond the ice Ih stability field. In Figure 8, principal

stresses in elastic shocks (■ and open symbols) are reduced to pressure (×) using equation (6) and compared to 100 and 263 K isotherms (solid lines), given by the Murnaghan equation [*Murnaghan*, 1944; *Jeanloz*, 1989],

$$P_T = \frac{K_{T0}}{K'_T} \left[ \left( \frac{V_0}{V} \right)^{K'_T} - 1 \right]. \quad (7)$$

The isothermal bulk modulus at zero pressure  $K_{T0}$  is derived from the intercept in the elastic  $U_S - \Delta u_p$  EOS, which defines the mean longitudinal wave speed,  $c_l = 3610 \text{ m s}^{-1}$ , and the intercept of the ice Ih deformation shock EOS (region 2) is fixed at the mean bulk wave speed,  $c_b = 3000 \text{ m s}^{-1}$  [*Petrenko and Whitworth*, 1999]. The scatter in measurements of the bulk wave speed is about  $100 \text{ m s}^{-1}$ . The inferred bulk moduli are 8.4 and 8.3 GPa at 100 and 263 K, respectively.

[36] The first derivative of the isothermal bulk modulus,  $K'_T$ , can be derived from the ice Ih deformation shock states using  $K'_T \simeq 4s - 1$  [e.g., *Ruoff*, 1967; *Jeanloz*, 1989], where  $s$  is the slope of the linear  $U_S - \Delta u_p$  fit.  $K'_T$  is  $3.0^{+3.2}_{-3.0}$  for  $s = 1.00 \pm 0.8$  (Table 3, region 2). Because the shock data in the ice Ih phase covers a small range of pressures,  $K_{T0}$  and  $K'_T$  are not strongly constrained. However, the inferred values for  $K_{T0}$  and  $K'_T$  (Table 4), derived here under uniaxial strain conditions, are in good agreement with static values [*Hobbs*, 1974; *Petrenko and Whitworth*, 1999].

### 3.4. Ice Ih Shocks

[37] The low-temperature shock experiments recorded the first observed steady deformational shock waves in the ice

**Table 4.** Parameters Used to Construct Reference Isotherms and Reference Isentropes<sup>a</sup>

Phase	$\rho_0$ , g cm <sup>-3</sup>	$K_{T_0}$ , GPa	$K'$ d $K_T$ /d $P$	$T_0$ , K
Ih <sup>b</sup>	0.93	8.4	3.0	100
VI <sup>c</sup>	1.30	13.08	6.8	230
VII <sup>d</sup>	1.46	21.1	4.4	300

<sup>a</sup>For reference isotherms, see equation (25); for reference isentropes, see section 3.5.  $K_{T_0} \sim K_{S_0}$  and  $dK_S/dP \sim dK_T/dP$  [Sotin *et al.*, 1998].

<sup>b</sup> $K_{T_0}$ ,  $K'$  derived from shock data.

<sup>c</sup> $K_{T_0}$ ,  $K'$  from Tulk *et al.* [1997].

<sup>d</sup> $K_{T_0}$ ,  $K'$  from Frank *et al.* [2004].

Ih structure. The ice Ih shocks are observed as the second wave in three-wave shock fronts, composed of an elastic shock precursor, deformation shock in the ice Ih structure, and transformation shock to ice VI (refer to auxiliary material, shots 1043, 1046, and 1047, and Figure 2a). The amplitude of the intermediate ice Ih shock appears to be dependent on the peak shock stress up to a limiting pressure of  $1.16 \pm 0.02$  GPa. At this point a cusp forms on the ice Hugoniot, similar to the 13 GPa cusp observed on the iron Hugoniot, derived from three-wave shock profiles corresponding to the HEL,  $\alpha$  deformation shock, and  $\alpha \rightarrow \epsilon$  transformation shock [Minshall, 1955; Bancroft *et al.*, 1956; Loree *et al.*, 1965].

[38] In our experiments with peak stresses in the range 0.4–0.5 GPa, steady ice Ih shock waves do not develop. The elastic precursor is followed by a decaying ice Ih deformation wave. Previous 263 K experiments also record decaying ice Ih shock waves (e.g., Figure 4 in Larson [1984] with peak stress of 0.295 GPa). Larson's decaying shock wave profiles are in good agreement with more recent shock attenuation experiments below 1 GPa conducted at an initial temperature of 255 K [Kato *et al.*, 2001]. At 100 K, we infer that steady ice Ih deformation shock Hugoniot measurements are possible only when the shock wave is supported by a subsequent transformation wave to ice VI. The ice Ih deformation shock region on the 100 K ice Hugoniot is bounded by the mean HEL (0.47 GPa) and the ice Ih deformation shock cusp at 1.16 GPa (Figure 8). At 263 K, the region is bound by the mean HEL (0.18 GPa) and the onset of transformation to ice VI at stresses above 0.6 GPa.

[39] Upon being shocked above the HEL, many minerals fail in a brittle manner and respond hydrodynamically. As in SiO<sub>2</sub> and other minerals, the 100 K ice Ih deformational shock states approach the hydrodynamic isotherm with increasing pressure (★, Figure 8). Hence, in the phase transformation regions of the Hugoniot (regions 2–5, above 1.16 GPa), we infer that the ice behaves hydrodynamically and the amplitude of the shock stress is equal to the hydrostatic pressure (also see section 3.8).

[40] The difficulty in development of a steady ice Ih deformation shock may be exacerbated by the failure mechanism in the elastic shock. At shock pressures just above the elastic limit, the shock wave propagates at an initial velocity less than the bulk sound speed in ice (subsonically). In the present and previous studies, ice Ih deformation shocks, steady and non-steady, display relatively long rise times in the shock fronts (see auxiliary material). The same phenomena is observed in AlN, where just above the HEL, the shock velocity is subsonic and the wave profile is plastic [Mashimo *et al.*, 1999; Rosenberg *et*

*al.*, 1991]. Mashimo *et al.* [1999] note that slip systems along macroscopic cracks may control brittle failure in AlN. If the failure mode increases heterogeneity in the material (e.g., by transformation faulting in shear bands), the low-amplitude shock following the elastic precursor will encounter scattering shear bands that increase the shock front rise time with propagation, resulting in decay of the shock amplitude and velocity.

[41] All ice Ih deformational shocks, steady and non-steady, achieve  $P - V$  states well beyond the ice Ih stability field (Figure 7). If the loss of shear strength is complete, ice Ih shock states fall within the liquid field when  $T_0 \sim 263$  K (not shown) and the ice VI field when  $T_0 \sim 100$  K (★). Hence ice Ih deformation shocks are not in thermodynamic equilibrium because of residual strength (see section 3.8).

### 3.5. Shock Temperatures

[42] Temperatures achieved along the 100 K and 263 K Hugoniots are shown in the  $P - T$  phase diagram (Figure 9). Areas corresponding to the five  $U_s - \Delta u_p$  EOS regions on the Hugoniot are shown as hatched and dotted areas. The stable crystalline phases (Ih-X) and liquid water are labeled in the inset  $P - T$  phase diagram for reference.

[43] Temperatures in the elastic shock and ice Ih deformation shock regions (1 & 2) on the ice Hugoniots remain near the initial temperature. Elastic shocks drive ice Ih out of its stability field, and the close agreement between the elastic shock states and hydrostatic isotherms indicates that the temperature increase is negligible. Similarly, because the ice Ih deformation shock states fall within uncertainty on the extrapolated 100 K isotherm at the 1.16 GPa cusp in Figure 8, the Hugoniot temperature in region 2 is assumed to be the initial temperature.

[44] At higher shock pressures, the large volume change associated with phase transformations results in rapid increase in temperature along the Hugoniot. Temperatures in hydrodynamic shock states, in regions 3 and above, are calculated by balancing the energy deposited by the shock upon compression to volume,  $V$ , with the sum of (i) the internal energy on a reference isentrope at  $V$ , (ii) a heating term at  $V$  from the isentrope to the Hugoniot, and (iii) the zero pressure energy difference between the Hugoniot and the reference isentrope. For simple systems without phase changes, the reference curve is usually centered at the same  $P - V - T$  point as the Hugoniot [e.g., Meyers, 1994, chap. 4].

[45] For H<sub>2</sub>O ice Hugoniots, the reference curve is matched to the phase in the shocked state, as illustrated by the points labeled  $A - D$  in Figure 10. In this example, a shock in the ice VII region of the Hugoniot is referenced to an ice VII isentrope at the same initial temperature. Equating the energy,  $E$ , along the two  $P - V$  paths from point  $A$  to  $B$ , gives

$$E_{AB} = E_{AD} + E_{DC} + E_{CB} \quad (8a)$$

$$0.5P_B(V_B - V_A) = (E_D - E_A) + \int_{V_D}^{V_C} P_S dV + \int_{T_C}^{T_B} c_v dT, \quad (8b)$$

where  $c_v$  is the specific heat capacity at constant volume of the phase in the shocked state and  $P_S$  is the reference isentrope. When  $c_v$  can be considered a constant, the shock

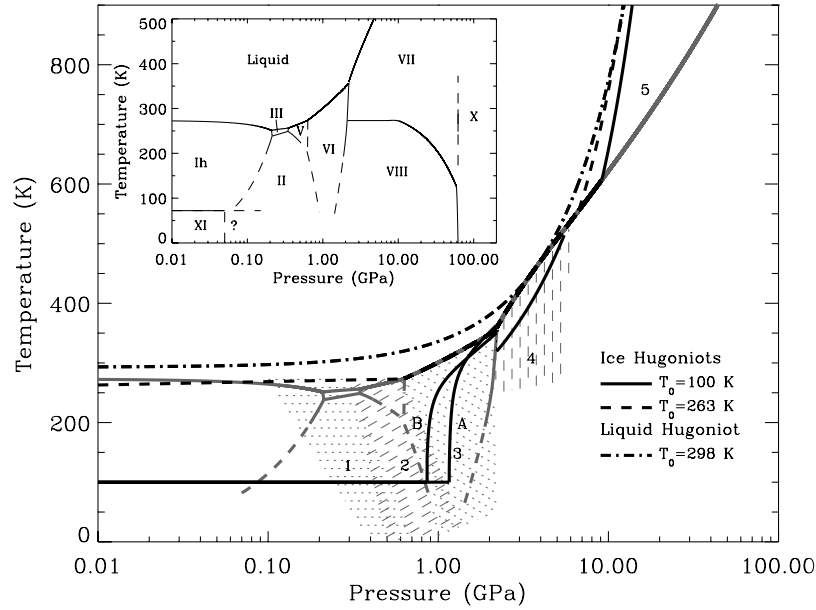


**Figure 9.** H<sub>2</sub>O phase diagram with 100 K and 263 K ice Hugoniots and 298 K liquid water Hugoniot. Note pressure scale is logarithmic for detail in low-pressure phases and inset shows expanded phase diagram. The pressure-temperature ranges of the 5 ice Hugoniot regions (Table 3) are noted by dotted and dashed areas. Two loci (A and B) are shown on the 100 K Hugoniot.

temperature,  $T_H$ , at point  $(P_H, V)$  is given in a general form as

$$T_H(V) = 0.5P_H(V - V_{0H})/c_v - (E_{0S} - E_{0H})/c_v - \frac{1}{c_v} \int_{V_{0S}}^V P_S dV + T_S, \quad (9)$$

where subscripts  $H$  and  $S$  denote the Hugoniot and reference isentrope, respectively, and subscript  $0$  refers to the initial

zero-pressure state.  $T_S$  denotes the temperature on the reference isentrope at  $V$ , given by the integral along the isentrope

$$T_S(V) = T_0 \exp\left(-\int_{V_0}^V \frac{\gamma}{V} dV\right), \quad (10)$$

where  $\gamma$  is the Mie-Grüneisen parameter of the phase in the shocked state.

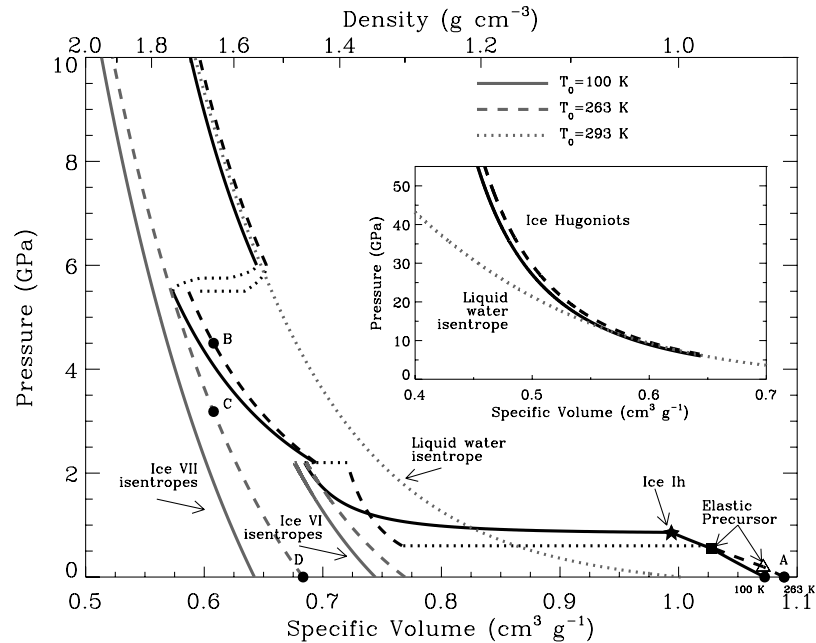


**Figure 10.** 100 K and 263 K ice Hugoniots (black lines) with reference curves for shock temperature calculations: 293 K liquid water, ice VI, and ice VII isentropes (gray lines). Locus B shown for the 100 K Hugoniot. High-pressure region referenced to liquid water isentrope (inset).



**Table 5.** Parameters Used to Calculate Shock Temperatures and Entropies

$T_0$ , K	Hugoniot Region	$\Delta E_0$ , kJ/kg	$P_{S,1}$ , GPa	$T_{S,1}$ , K	$S_{S,1}$ , J/(kg K)
100	3 – VI (A)	–2.8	1.16	120	856
100	3 – VI (B)	–2.8	0.86	141	856
100	4 – VII	–65.5	2.2	319	2401
100	5 – VII-L	–65.5	2.2	284	2031
100	5 – L	670.1	0.0	293	3792
263	3 – VI	–6.9	0.62	273	2530
263	4 – VII	–106.2	2.2	358	3238
263	5 – VII-L	–106.2	2.2	358	2967
263	5 – L	433.8	0.0	293	3792

[46] The zero pressure energy difference,  $\Delta E_0 = E_{0S} - E_{0H}$ , is calculated from the entropy offset,  $\Delta S_0$ , between the base of the Hugoniot and the isentrope by

$$\Delta E_0 = T_0 \Delta S_0. \quad (11)$$

Values for  $\Delta E_0$  are given in Table 5.  $\Delta S_0$  is calculated from  $c_p$ , the heat capacity at constant pressure, for each phase.  $c_v$  and  $c_p$  have not been measured for ices VI and VII over most of the temperature and pressure range of interest here. Where measurements are available, the ratio  $K_S/K_T = c_p/c_v$  is approximately one (within 3% [Sotin *et al.*, 1998]), and we assume  $c_p = c_v$  for ices VI and VII.

[47] To calculate the shock temperatures in the ice VI and VII regions, isentropes based at the same initial temperature,  $T_0$ , as the Hugoniot are used as the reference curves. Because  $K_S \sim K_T$ , the isentropes are derived using the method described in sections 3.7.1 and 3.7.2 for calculating isotherms for each phase.

[48] The heat capacity of ice Ih,  $c_{p,Ih}$ , is taken from *Giauque and Stout* [1936] and *Haida *et al.** [1974]. Because of the lack of direct measurements at low temperatures, we use the same heat capacity for ice VI as ice Ih, which provides good agreement with the entropy of the ice VI phase boundary (section 3.6). We fit the ice Ih heat capacity data with a 6th order polynomial that extrapolates the data linearly to 500 K for the shock temperature calculations, given by

$$c_{p,Ih} = -47.9 + 9.59T + 0.0125T^2 - 2.78 \times 10^{-4}T^3 + 1.35 \times 10^{-6}T^4 - 2.65 \times 10^{-9}T^5 + 1.86 \times 10^{-12}T^6, \quad (12)$$

in  $\text{J kg}^{-1} \text{K}^{-1}$ , with  $T$  in K. The root mean square difference between the fit and the data is less than  $20 \text{ J kg}^{-1} \text{K}^{-1}$ . The ice VII heat capacity is calculated using the Debye function, where

$$c_{v,VII} = c_{\max} \mathcal{D}\left(\frac{T_D}{T}\right), \quad (13)$$

$c_{\max}$  is the high-temperature limiting value,  $T_D$  is the Debye temperature, and  $\mathcal{D}(T_D/T)$  is the normalized third order Debye function,

$$\mathcal{D}\left(\frac{T_D}{T}\right) = \frac{3}{(T_D/T)^3} \int_0^{T_D/T} \frac{x^4 e^x}{(e^x - 1)^2} dx. \quad (14)$$

For ice VII, the two parameters,  $c_{\max} = 4600 \text{ J kg}^{-1} \text{K}^{-1}$  and  $T_D = 850 \text{ K}$ , are constrained by the fitted heat capacity between 300–700 K from *Fei *et al.** [1993] and the entropy at the phase boundary. Note that the high-temperature limit for ice VII exceeds the Dulong-Petit limit, and  $T_D$  is an empirical fit as ice is not well described by a single Debye temperature [cf. *Hobbs*, 1974].

[49] As  $K_S \sim K_T$ , the temperature increase on the reference isentropes of ices VI and VII is negligible (equation (10)). On the basis of the thermodynamic relation,  $\gamma = \alpha K_T V / c_v$ , where  $\alpha$  is the volume coefficient of thermal expansion (given in section 3.7.1), the temperature change is less than 10 K.

[50] In Figure 9, the shock temperature calculations include the average HEL and ice Ih deformation shocks (labeled symbols in Figure 10) in the calculation of the energy in the final shock state, which is derived by multiple applications of  $0.5(P_1 + P_2)(V_1 - V_2)$ . Note that shock temperatures are calculated along both locus A and B in the ice VI region on the 100 K Hugoniot (see section 3.7.1).

[51] For  $T_0 = 100 \text{ K}$ , the intermediate ice Ih shock state lies above a simple Rayleigh line connecting the initial and final shock states in the ice VI field, resulting in the rapid increase in temperature along the Hugoniot (region 3, Figure 9). Shock temperatures lie below the melting curve for shock pressures below 5.5 GPa (regions 1–4). In region 5, the latent heat of melting buffers the temperature until shock pressures above 9.2 GPa are achieved and the Hugoniot enters the liquid water field.

[52] For  $T_0 = 263 \text{ K}$ , all shock temperatures in regions 3 and 4 lie on the melting curve, where the shock state is a mixture of liquid water and a high-pressure phase of ice. When the temperature on the ice Hugoniot is buffered by melting, the shock temperature is equal to the equilibrium boundary temperature. The temperature,  $T_b$ , at pressure,  $P_b$ , along the melting curve, is given by

$$P_b = P_{b,0} + c_1 \left[ \left( \frac{T_b}{T_{b,0}} \right)^{c_2} - 1 \right], \quad (15)$$

where  $P_{b,0}$ ,  $T_{b,0}$ ,  $c_1$ , and  $c_2$  are constants fit to experimental data, given in Table 6 [Sotin *et al.*, 1998; Frank *et al.*, 2004].

[53] Above 9.2 and 6.7 GPa for  $T_0 = 100$  and 263 K respectively, the latent heat of melting is overcome and the ice Hugoniot crosses into the liquid water stability field. At these pressures, the reference curve is the liquid water isentrope based at 293 K (Figure 10 inset) rather than a solid ice isentrope. Pressure and energy along the liquid water isentrope,  $P_i$  and  $E_i$ , are calculated iteratively from the pressure and energy on the 293 K liquid water Hugoniot,  $P_H$

**Table 6.**  $P - T$  Phase Boundary Constants Used in Equation (15)

Phase Boundary	$P_{b,0}$ , MPa	$T_{b,0}$ , K	$c_1$ , MPa	$c_2$ , –
L – Ih <sup>a</sup>	0	273.16	–395.2	9.0
L – VI <sup>a</sup>	625	273.31	707	4.46
L – VII <sup>b</sup>	2170	355	764	4.32

<sup>a</sup>Sotin *et al.* [1998].

<sup>b</sup>Frank *et al.* [2004].



and  $E_H$  respectively, following the method of *McQueen* [1991]:

$$P_i = \frac{P_H - (\gamma/V)_i(E_H - E_{i-1} + P_{i-1}\Delta V/2)}{1 + (\gamma/V)_i(\Delta V/2)}, \quad (16)$$

$$E_i = E_{i-1} - (P_i + P_{i-1})(\Delta V/2), \quad (17)$$

where  $\Delta V = V_i - V_{i-1}$  and  $\gamma$  is the liquid water Mie-Grüneisen parameter. The liquid water Hugoniot data [Lawton and Skidmore, 1955; Skidmore and Morris, 1962; Ahrens and Ruderman, 1966; Bakanova et al., 1976; Marsh, 1980; Volkov et al., 1980; Mitchell and Nellis, 1982; Sharipdzhanov et al., 1984; Nagayama et al., 2002] are best fit by the formulation of *Woolfolk et al.* [1973],

$$U_S = c_0 a_0 + c_0(1 - a_0) \exp(-a_1 u_p / c_0) + a_2 u_p, \quad (18)$$

where  $c_0 = 1480 \text{ m s}^{-1}$  is the zero pressure sound velocity, and  $V_0 = 1.0017695 \times 10^{-3} \text{ m}^3 \text{ kg}^{-1}$  at 293 K [Dorsey, 1940]. The  $a$  coefficients are found by least squares fit to be  $a_0 = 2.3822 (\pm 0.0013)$ ,  $a_1 = 0.78311 (\pm 0.00083)$ , and  $a_2 = 1.13443 (\pm 0.00025)$  for  $u_p < 8710 \text{ m s}^{-1}$  (114 GPa). We derive the liquid water  $\gamma$  from double shock measurements and porous ice shock data (S. T. Stewart and T. J. Ahrens, Collisions between porous icy bodies in the solar system, manuscript in preparation, 2005), where a least squares fit to the standard formulation of

$$\gamma = \gamma_0 (V/V_0)^q \quad (19)$$

gives  $\gamma_0 = 0.85 \pm 0.12$  and  $q = 0.21 \pm 0.17$ .

[54] The zero-pressure energy difference between the ice Hugoniot and the liquid water reference isentrope is given by

$$\Delta E_0 = \int_{T_0}^{273} c_{p, \text{lh}} dT + L + \int_{273}^{T_{0S}} c_{p, \text{liquid}} dT, \quad (20)$$

where  $T_{0S} = 293 \text{ K}$  is the base temperature on the reference isentrope and the latent heat of melting ice Ih,  $L$ , is  $333.5 \text{ kJ kg}^{-1} \text{ K}^{-1}$  [Petrenko and Whitworth, 1999]. The heat capacity of liquid water,  $c_{p, \text{liquid}}$ , is taken from the tabulated values at 1 bar [Wagner and Pruss, 2002]. The calculated values for  $\Delta E_0$  are given in Table 5.

[55] There are no shock temperature measurements on the liquid water Hugoniot at pressures below 30 GPa (corresponding to 2000 K). The heat capacity of liquid water is not constant up to pressures of 1 GPa [Wagner and Pruss, 2002], and measurements are not available over the pressure and temperature range required for equation (8b). Therefore, in Figure 9, the liquid water shock temperatures,  $T_{H, \text{liquid}}$  (in K), are interpolated between low-pressure calculations [Snay and Rosenbaum, 1952] and data (between 30 and 80 GPa [Kormer, 1968; Lyzenga et al., 1982]) as a function of shock pressure (in GPa) by

$$T_{H, \text{liquid}}(P) = 293(\pm 5) + 42.4(\pm 4.2)P + 0.64(\pm 0.4)P^2 - 8(\pm 11) \times 10^{-3}P^3 + 4.0(\pm 8.5) \times 10^{-5}P^4. \quad (21)$$

In Figure 9, the liquid water Hugoniot intersects the phase boundary between 3 and 4 GPa but does not enter the ice VII field, in agreement with *Rice and Walsh* [1957] and *Dolan* [2003].

[56] Here, we use the shock temperature data for liquid water to solve for  $c_{v, \text{liquid}}$  as a function of temperature. From equation (9),  $c_{v, \text{liquid}}$  rises linearly from 3535 to 4025  $\text{J kg}^{-1} \text{ K}^{-1}$  between 2000 and 5270 K (30 and 80 GPa on the liquid water Hugoniot). Below 2000 K, we adopt a constant  $c_{v, \text{liquid}} = 3420 \pm 60 \text{ J kg}^{-1} \text{ K}^{-1}$ , inferred from the interpolated shock temperatures (equations (21) and (9)). This average value also agrees well with the extrapolation of the heat capacity values, derived from the shock temperature data, below 2000 K. On the 293 K liquid water Hugoniot between 7–30 GPa, the mean absolute difference between the interpolated shock temperatures and calculations based on a constant  $c_{v, \text{liquid}}$  is only 11 K. The constant value of  $c_{v, \text{liquid}}$  is used to calculate the shock temperatures in the liquid water region on the ice Hugoniots.

[57] The calculated ice Hugoniot temperatures in the liquid region intersect the ice VII melting curve at 6.7 GPa (556 K) for  $T_0 = 263 \text{ K}$  and 9.2 GPa (607 K) for  $T_0 = 100 \text{ K}$ . The temperatures on the 100 and 263 K ice Hugoniots cross above the 293 K liquid water Hugoniot (equation (21)) at 11.4 GPa (848 K) and 20.2 GPa (1350 K), respectively. The cross-over pressures are sensitive to the exact formulation of the Hugoniots, which are steep in this pressure range and can vary by as much as 2 GPa. The *Woolfolk et al.* [1973] formulation (equation (18)) provides a better fit to the liquid water shock data between 0 and 50 GPa than a linear or quadratic function between shock velocity and particle velocity.

[58] The shock temperatures on the 100 and 263 K ice Hugoniots are summarized in Table 7. The estimated errors on the calculated shock temperatures, away from the phase boundaries, are a few 10's K below about 10 GPa. Extrapolations to high pressures, using a constant heat capacity of liquid water, should be used with caution. Previous studies have used the liquid water Hugoniot as a reference to derive solid (nonporous) and porous ice Hugoniots and calculate ice shock temperatures [e.g., Bakanova et al., 1976; Ahrens and O'Keefe, 1985]. On the solid ice Hugoniot, liquid water is a robust reference at pressures where the shock state is pure liquid, and derivation of thermodynamic properties of liquid water from the solid ice Hugoniot [e.g., Bakanova et al., 1976] is only valid above about 10 GPa.

### 3.6. Entropy on the Hugoniot

[59] The 100 and 263 K ice Hugoniots are shown in the pressure-entropy ( $P - S$ ) plane, as solid and dashed lines in Figure 11, respectively, with a partial phase diagram of H<sub>2</sub>O. The zero-pressure entropy of ice Ih is 884 and 2197  $\text{J kg}^{-1} \text{ K}^{-1}$  at 100 and 263 K, respectively, calculated from  $c_{p, \text{lh}}$  (equation (12)) and the zero point entropy of ice Ih (189.2  $\text{J kg}^{-1} \text{ K}^{-1}$ ) [Petrenko and Whitworth, 1999]. The critical entropies for incipient (IM) and complete (CM) melting at the triple point pressure are 2290 and 3510  $\text{J kg}^{-1} \text{ K}^{-1}$  [Petrenko and Whitworth, 1999]. The gray region in Figure 11 denotes the entropy difference between the solid phases of ice and liquid water. The phase boundaries are constructed from latent

**Table 7.** Shock Temperature Fits on the 100 and 263 K Ice Hugoniots

$T_0$ , K	Hugoniot Region	Pressure $P_H$ , GPa	Temperature <sup>a</sup> $T_H$ , K
100	2 – Ih	0 – ~1	100
100	3 – VI (A)	~1.2 – 2.2	$-111 + 421P_H - 94.3P_H^2$
100	3 – VI (B)	~1 – 2.2	$97.7 + 201P_H - 39.9P_H^2$
100	4 – VII	2.2 – 5.5	$171 + 71.1P_H - 1.58P_H^2$
100	5 – VII-L	5.5 – 9.2	$323 + 45.0P_H - 1.53P_H^2$
100	5 – L	9.2 – 50	$14.7 + 59.6P_H + 0.341P_H^2$
263	2 – Ih	0 – 0.6	263
263	3 – VI	0.6 – 2.2	$222 + 92.6P_H - 14.9P_H^2$
263	4 – VII	2.2 – 5.0	$132 + 128P_H - 10.7P_H^2$
263	5 – VII-L	5.0 – 6.7	$286 + 56.6P_H - 2.45P_H^2$
263	5 – L	6.7 – 50	$111 + 60.9P_H + 0.355P_H^2$

<sup>a</sup> $P_H$  in GPa.

heat and volume change measurements (Bridgman's data compiled by Dorsey [1940]) and the  $P - V - T$  equations of state for ices VI and VII (derived in sections 3.7.1 and 3.7.2). Note that the entropy change between ice VII and liquid water is extrapolated above about 3 GPa, shown with dotted lines on the phase boundary.

[60] On both the 100 and 263 K Hugoniots, the elastic and ice Ih deformation shocks are approximately isentropic, on the basis of the agreement with the extended isothermal compression curves. Although there may be partial melting in the ice Ih region along the 263 K Hugoniot, the initial entropy indicates that the shocked state will remain primarily a solid phase. 263 K elastic and ice Ih deformational shocks ( $P < 0.6$  GPa) enter the liquid phase boundary (shaded region, Figure 11) with ices Ih, III, and V. We infer that the solid phase in this region is ice Ih by the density of the shocked state, which follows the extended ice Ih isotherm (Figure 8). Hence the measured density does not indicate any (partial) transformation to the denser ices III or V, and the temperatures in the ice Ih region of the Hugoniot do not follow the equilibrium phase boundary. On the 100 K Hugoniot, the close agreement between the steady ice Ih deformation shock states and the 100 K isotherm (Figure 8) indicates that the entropy increase in the deformational shocks is not large enough to initiate melting of ice Ih. On the sub-microsecond time scales of the shock compression experiments, the ice Ih structure is driven far outside of its thermodynamic stability field.

[61] At pressures above the ice Ih region, the entropy in the shock state,  $S_H(V)$ , is calculated from the reference isentrope plus a term for the temperature difference between the isentrope and the Hugoniot at volume,  $V$ , where [e.g., Zel'dovich and Raizer, 2002]

$$S_H(V) = S_{S,1} + \int_{T_{S,1}}^{T_H(V)} \frac{c_v}{T} dT. \quad (22)$$

The entropy is calculated separately in each Hugoniot region using the heat capacity,  $c_v$ , and reference isentrope of the shocked state. The reference isentrope is defined at the base pressure,  $P_{S,1}$ , and temperature  $T_{S,1}$ , given in Table 5.

[62] When the temperature at the base of the Hugoniot segment is less than the melting curve, the reference entropy,  $S_{S,1}$ , is calculated by integrating the heat capacity of the high-pressure phase,  $c_p$ , from the temperature on the

liquid water phase boundary,  $T_b$ , to the temperature at the reference point,  $T_{S,1}$ , at  $P_{S,1}$ , such that

$$S_{S,1} = S_b + \int_{T_b}^{T_{S,1}} \frac{c_p}{T} dT, \quad (23)$$

where  $S_b$  is the entropy of the solid on the phase boundary. In the cases where the calculated shock temperature,  $T_{H,calc}$  (equation (8b)), is larger than the temperature on the melting

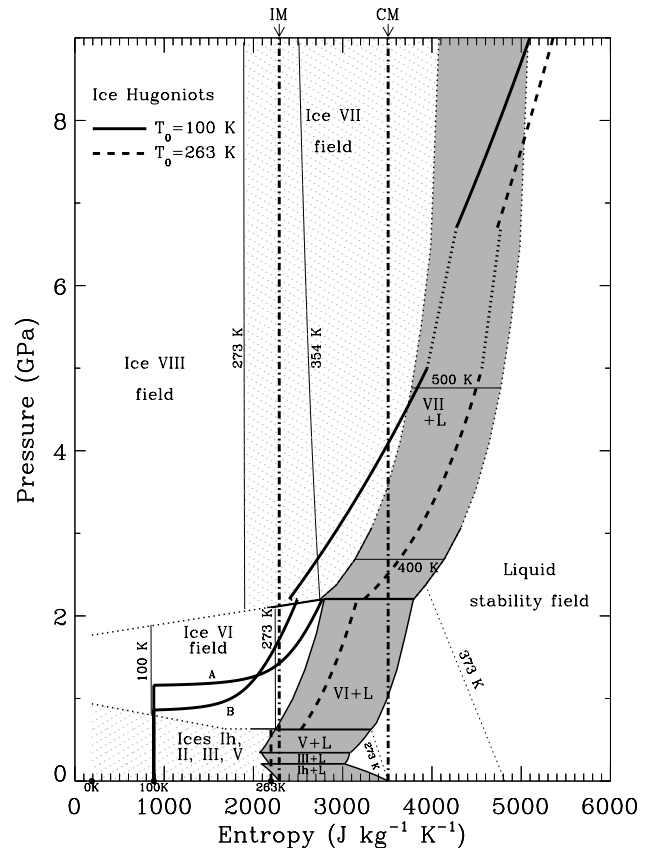


**Figure 11.** The 100 K and 263 K ice Hugoniots and partial pressure-entropy H<sub>2</sub>O phase diagram (revised from Stewart and Ahrens [2003]). IM and CM denote critical entropies for incipient and complete melting upon release to ambient pressure. Two loci (A and B) are shown on the 100 K Hugoniot.

curve,  $T_{S,1}$  equals  $T_b$  at  $P_{S,1}$  and the reference entropy includes partial melting to liquid water, where

$$S_{S,1} = S_b + \int_{T_b}^{T_{H,calc}} \frac{c_p}{T} dT. \quad (24)$$

The temperature on the isentrope,  $T_S(V)$ , is calculated from equation (10).

[63] In Figure 11, the entropy on the 263 K ice Hugoniot follows the phase boundary with liquid water in the ice VI and ice VII regions. The 100 K ice Hugoniot intersects the entropy on the phase boundary around 4.5 GPa. The discrepancy between the intersection of the Hugoniot with the melting curve derived from temperature (5.5 GPa) and entropy (4.5 GPa) are due to the large uncertainty in the extrapolated entropy change on the ice VII melting curve. The values derived from the shock temperature are more robust. Similarly, the 263 K ice Hugoniot enters the liquid water stability field at a higher pressure on the  $P - S$  diagram (7.7 GPa) than on the  $P - T$  diagram (6.7 GPa), and the temperature-derived value is recommended. On both Hugoniots, the entropy in region 5 is derived in two segments, using an ice VII reference isentrope along the phase boundary and a liquid water isentrope in the liquid stability field. The entropy on the two segments intersect at the pressure where the Hugoniots cross into the liquid water stability field, as derived from the shock temperatures, providing a consistency check between the different reference isentropes.

[64] The dotted region on the Hugoniots between 5 and 6.7 GPa corresponds to the transition to region 5 on the Hugoniot, when the elastic precursor is overdriven. On both Hugoniots, the discontinuity at the top of the ice VI region reflects the change from an ice VI to an ice VII reference isentrope. Due to the intermediate ice Ih shock, the temperatures and entropy along the ice VI region of the 100 K Hugoniot rapidly approach the melting curve.

[65] The shock pressures required for melting upon release are derived using the entropy method. Assuming isentropic release from the shock state, the points where the Hugoniot cross the entropies for incipient (IM) and complete (CM) melting of ice at ambient pressure define the critical shock pressures for melting.

[66] Along the 263 K Hugoniot, the entropy is larger than the critical value for incipient melting (vertical dot-dashed line labeled IM in Figure 11) at pressures greater than about 0.6(±0.05) GPa. Therefore shocks to the ice VI region on the Hugoniot will partially melt upon release to 1 bar pressure. The critical pressure for IM is coincident with the onset of shock-induced transformation to ice VI and the ice VI phase boundary at 0.632 GPa; hence the critical pressure is sensitive to the exact onset of the phase transformation on the Hugoniot. The quoted error of ±0.05 GPa is derived from two experiments from *Larson et al.* [1973], showing no phase transformation at 0.48 GPa and the ice VI transformation at 0.69 GPa.

[67] The entropy along the ice VII region of the 263 K Hugoniot is larger than the critical entropy for complete melting (CM) above 2.5 (±0.1) GPa. The critical pressure is sensitive to the specific heat capacity of ice VII, which is

constrained near the phase boundary by *Fei et al.* [1993]. A 25% error in the heat capacity leads to less than 0.1 GPa error in the critical pressure.

[68] In the ice VI region on the 100 K Hugoniot, the entropy for incipient melting is reached above 1.7 GPa following locus B, where the intermediate ice Ih shock has an amplitude of 0.86 GPa. Along locus A, where the ice Ih shock travels through the cusp at 1.16 GPa, incipient melting is reached at 1.4 GPa. Changing the heat capacity of ice VI by 10% changes the critical pressure by 0.2 to 0.3 GPa. Because the variable amplitude of the intermediate ice Ih shock contributes to the entropy in the ice VI region, we recommend an average critical pressure of  $1.6 \pm 0.3$  GPa.

[69] On the 100 K ice Hugoniot will melt completely upon release from shock pressures above  $4.1 \pm 0.3$  GPa. A 25% error in the heat capacity induces a 0.3 GPa error in the critical pressure. The implications of the new critical pressures for shock-induced melting are discussed in section 4.

[70] The entropy of incipient and complete vaporization at 1 bar are 4817 and 10864 J kg<sup>-1</sup> K<sup>-1</sup>, respectively [*Wagner and Pruss*, 2002]. The critical pressure (and shock temperature) for incipient vaporization upon release are  $9.0 \pm 0.2$  GPa ( $600 \pm 70$  K) and  $7.0 \pm 0.2$  GPa ( $570 \pm 70$  K) on the 100 and 262 K ice Hugoniots, respectively, for  $c_{v,liquid} = 3420$  J kg<sup>-1</sup> K<sup>-1</sup>. Assuming  $c_{v,liquid} = 2500$  J kg<sup>-1</sup> K<sup>-1</sup> (at high temperatures (e.g., *Wagner and Pruss*, 2002)), the critical pressures increase by 0.2 GPa. The present methods for calculating shock temperature and entropy do not capture the complexity of supercritical water; hence extrapolations to high pressures should be used with caution. For example, with  $c_{v,liquid} = 3420$  J kg<sup>-1</sup> K<sup>-1</sup>, the critical pressure (and shock temperature) for complete vaporization upon release are 55 GPa (4300 K) and 53 GPa (4250 K) on the 100 and 262 K ice Hugoniots, respectively. Assuming  $c_{v,liquid} = 2500$  J kg<sup>-1</sup> K<sup>-1</sup>, the critical pressures increase by about 30 GPa and 5200 K.

### 3.7. Transformation Shocks

#### 3.7.1. Ice VI

[71] The shock-induced phase transformation to ice VI has been previously identified by *Gaffney and Ahrens* [1980] and *Larson* [1984] from the large volume compression on the Hugoniot, >40%, at pressures above 0.6 GPa. On the 263 K Hugoniot, the transition to the ice VI region is clearly associated with the equilibrium phase boundary at 0.632 GPa (Figures 9 and 11).

[72] An unusual feature of the  $T_0 = 100$  K Hugoniot is that its volume is not single valued over the pressure range 0.6–1.2 GPa, corresponding to the regions of ice Ih deformation shocks and ice VI transformation shocks. The degenerate Hugoniot region is illustrated by the two loci of shock states, labeled A and B in Figure 5.

[73] The A locus corresponds to peak shock states above 1.16 GPa that pass through the ice Ih shock cusp. The locus of shock states labeled B in Figure 5 is based on one experiment (1046, denoted by (★)), with a peak shock stress of 1.03 GPa and intermediate ice Ih shock amplitude of 0.86 GPa. Locus B is representative of final shock stresses between 0.6 and 1.16 GPa, where ice VI forms on the low-temperature Hugoniot with an intermediate ice Ih shock. We suggest that the amplitude of the ice Ih



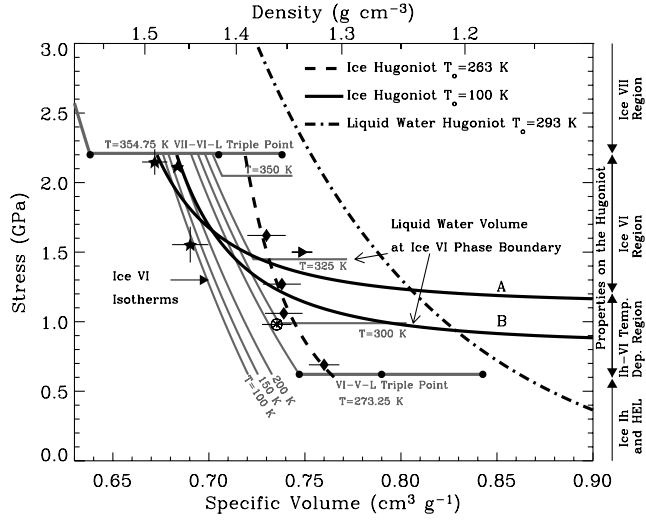


**Figure 12.** Ice VI Hugoniot region and ice VI isotherms with ice VII, liquid water, and ice V equilibrium phase boundaries. VII-VI-L and VI-V-L triple points (●) indicate volume differences between phases. Ice VI isotherms extend to liquid water phase boundary volume (horizontal segments). For  $T_0 = 263$  K, ice VI transformation shock states (dashed line, ♦ ►) lie in liquid water-ice VI coexistence region. For  $T_0 = 100$  K, data (★) are consistent with pure ice VI. Two loci (labeled A and B) shown on 100 K Hugoniot (Figure 5).

shock will scale with the final shock stress up to the observed 1.16 GPa limit.

[74] The shock data are shown with ice VI isotherms and the ice VI-liquid water phase boundary in Figure 12. Triple points [cf. *Petrenko and Whitworth*, 1999], VI-V-L and VII-VI-L, are horizontal lines in the  $P - V$  plane where the ● denotes the volume for each phase. The ice II and VIII phase boundaries are not shown. The volume differences at the ice VI-liquid water phase boundary and triple points are from *Dorsey* [1940].

[75] Isotherms are constructed using the formulation presented in *Fei et al.* [1993] and *Frank et al.* [2004], from a reference isotherm,  $T_{ref}$ , and model for the volume thermal expansion coefficient,  $\alpha$ . An isotherm at  $T$  is given by

$$V(P, T) = V(P, T_{ref}) \left[ \exp \left( \int_{T_{ref}}^T \alpha(P, T) dT \right) \right]_P. \quad (25)$$

We use the experimental 230 K isotherm for ice VI as the reference (Table 4). The linear thermal expansion coefficient is nearly constant at  $10^{-5} \text{ K}^{-1}$  between 140–200 K, on the basis of measurements at 1.054 GPa between 0–200 K by *Mishima et al.* [1979]. Without measurements at different pressures, we estimate  $\alpha$  for ice VI with the same formulation as *Frank et al.* [2004] for ice VII:

$$\alpha(P, T) = \alpha_0(T) \left( 1 + \frac{K'_{T0}}{K_{T0}} P \right)^{-\eta}, \quad \text{where} \quad (26a)$$

$$\alpha_0(T) = a_0 + a_1 T. \quad (26b)$$

$\alpha_0(T)$  is the zero-pressure thermal expansion coefficient. The constants derived by *Frank et al.* [2004] for ice VII agree well with the limited ice VI data and the phase boundary volumes are consistent with measurements of *Dorsey* [1940]. The thermal expansion values used for both ice VI and VII are  $a_0 = -4.2 \times 10^{-4} \text{ K}^{-1}$ ,  $a_1 = 1.56 \times 10^{-6} \text{ K}^{-2}$ , and  $\eta = 1.1$ .

[76] In Figure 12, the shock measurements with  $T_0 = 263$  K (♦ ►) do not fall in the ice VI stability field, but lie within the ice VI-liquid water phase boundary, indicating incomplete transformation to ice VI on the Hugoniot (dashed line). *Larson* [1984] inferred pure ice VI in this region of the Hugoniot by comparison to the 263 K isotherm (see his Figure 8). However, the temperature, entropy and volume along the Hugoniot indicate that this region is a mixture of ice VI and liquid water.

[77] The volumes of the  $T_0 = 100$  K data lie within the ice VI field (★, Figure 12), indicating pure ice VI in the shock state. There is a slight disagreement between the  $P - V$  isotherms and the calculated shock temperatures, which may be due to the uncertainties in the equation of state of ice VI. The 100 K Hugoniot (solid lines A and B in Figure 12) crosses the ice VI isotherms with negative  $dT/dP$ , suggesting that, at pressures just above the intermediate ice Ih shock, there is incomplete transformation to ice VI. The appearance of negative  $dT/dP$  along a single shock locus is an artifact of the multi-valued nature of this region on the Hugoniot, and both entropy and temperature increase with increasing shock pressure.

### 3.7.2. Ice VII

[78] The shock data between 2.2 and 20 GPa are shown together with ice VII isotherms and the ice VII-liquid water phase boundary in Figure 13. The ice VIII phase boundaries are not shown, and ice VII isotherms have been extrapolated out of the equilibrium field to lower temperatures. Note the 298 K liquid water Hugoniot approaches the ice VII-liquid

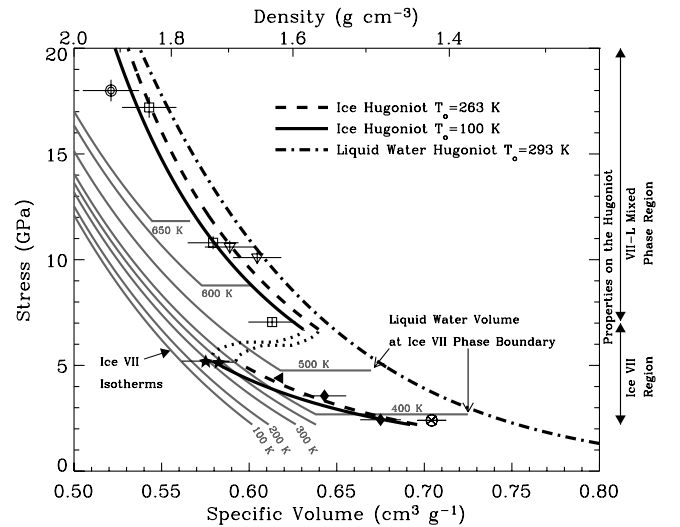


**Figure 13.** Ice VII Hugoniot region and ice VII isotherms with ice VI and liquid water equilibrium phase boundaries. VII-VI-L triple point (●) indicates volume differences between phases and ice VII isotherms extend to liquid water phase boundary volume (horizontal segments). ★, data from  $T_0 = 100$  K; all other symbols from  $T_0 = 263$  K.

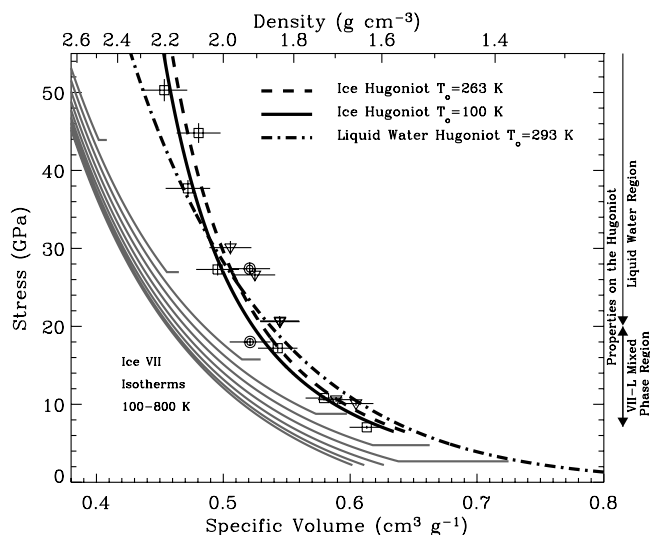


**Figure 14.** Liquid water region on ice Hugoniot (>6 GPa) and ice VII isotherms. Hugoniot states are pure liquid above 7.7 and 10.1 GPa for  $T_0 = 263$  and 100 K, respectively. All shock data obtained from  $T_0 = 263$  K.

water  $P - V$  boundary near 4 GPa, in the region bounded by the arrows denoting the liquid water volume at the phase boundary. The discontinuity (dotted lines in Figure 13) along the ice Hugoniots between 5.5–6 GPa correspond to shock waves traveling near the longitudinal wave speed, which have previously been confused with the elastic precursor.

[79] The  $P - V - T$  equation of state for ice VII has been well defined in our region of interest by *Frank et al.* [2004]. We use the reference isotherm at  $T_{ref} = 300$  K (Table 4) and the thermal expansion model presented in the previous section. In Figure 13, the volume difference at the liquid water phase boundary is taken from *Dorsey* [1940] and extrapolated outside the measured range.

[80] As predicted from the shock temperature calculations between 2.2 and 5.5 GPa, the  $T_0 = 263$  K shock data (◆ ◀) lie in or near the ice VII and liquid water phase boundary. In this region, both the 100 K and 263 K Hugoniots cross successively lower isotherms with increasing shock pressure, indicating different mixed assemblages of ice VII and liquid water in the shock states. With increasing pressure along the 100 K Hugoniot, the shock state approaches nearly pure ice VII. On the 263 K Hugoniot, a mixture of ice VII and liquid water is inferred from the temperatures and entropies attained in the shock state.

### 3.7.3. Liquid Water

[81] At pressures above 6 GPa ( $\Sigma u_p \geq 1590$  m s<sup>-1</sup>, region 5), the shock velocities are greater than the longitudinal wave speed and a single wave shock front propagates through ice. The new fit to the liquid water region on the ice Hugoniot (Table 3) agrees well with the high-pressure region of the temperate ice Hugoniot published by *Gaffney* [1985]. Figure 14 presents the ice shock data above 6 GPa together with ice VII isotherms up to 800 K, the ice VII-liquid water phase boundary, and the liquid water Hugoniot. In this region, the offset between  $T_0 = 100$  and 263 K is dominated by the difference in initial volume.

[82] Just above 6 GPa, the shock temperatures and volumes indicate that the Hugoniot contains a mixture of

ice VII and liquid. On the basis of the shock temperatures, the 100 and 263 K ice Hugoniots cross the ice VII-liquid phase boundary and enter the liquid field above shock pressures of 6.7 and 9.2 GPa, respectively (Figure 13), in good agreement with the  $P - V$  diagram.

[83] In Figure 14, the ice Hugoniots cross the liquid water Hugoniot between 25 and 30 GPa, at pressures larger than derived from the shock temperatures (11 to 20 GPa). The discrepancy is probably due to the sensitivity to the exact formulation of the Hugoniot and the assumption of a constant  $c_{v,liquid}$ . The ice Hugoniot crosses the liquid water Hugoniot because ice Ih has a larger initial volume than liquid water, which results in higher energy in the shock state at a given compressed volume.

[84] Above 0.6 GPa, in the ice VI, ice VII and liquid water regions, the transformations along the Hugoniot agree very well with equilibrium phase boundaries and support the idealized thermodynamic treatment for the calculation of shock temperatures and entropies.

### 3.8. Release From Shock States

[85] Shocked materials, that either retain or lose strength, are released to ambient pressure by a spreading rarefaction wave propagating with a maximum velocity corresponding to the isentropic longitudinal or bulk sound velocity in the shocked state. The release wave velocity constrains the rheology of the shocked state, and the release path prescribes the reversible energy of the shock state.

[86] Shock loading and release paths in ice are displayed with the shock Hugoniot in Figure 15, where data from this work and previous studies have been combined. In Figure 15, the major regions along the Hugoniot (thick lines) are not connected (as in Figure 5) for clarity, the initial states are denoted by filled black circles, and the other symbols correspond to the source data and indicate the peak shock state. Release isentropes fall into three regimes: A. Shocks to the ice Ih region follow stress-volume release paths below the Hugoniot, indicating possible elastic-plastic behavior. Note that the shock wave decayed slightly between gauges in the three lowest pressure experiments, and the peak stress state lies well below the Hugoniot. B. After shock transformation to ice VI or VII (0.6–5.5 GPa), ice unloads along the Hugoniot, following paths that appear to be a mixture of liquid water and ice VI or VII. This is also the pressure range for shock-induced melting upon release. C. Release paths after shock transformation to liquid water (>6 GPa) lie above the Hugoniot.

[87] Release path information has been obtained using three methods, which are denoted graphically in Figure 15: (1) Two or more embedded stress or particle velocity gauges record the full release wave profile. The  $\sigma - V$  release paths were derived from Lagrangian analysis and reproduced as curves with no terminal arrows in Figure 15. The experimental geometries of release wave measurements from different studies are described in the auxiliary material.

[88] (2) Release wave arrival times (this work) define the sound speed  $c_r$  on the Hugoniot. The initial slope of the isentropic release path off the Hugoniot is

$$c_r = V \sqrt{-\left(\frac{dP}{dV}\right)_s}, \quad (27)$$



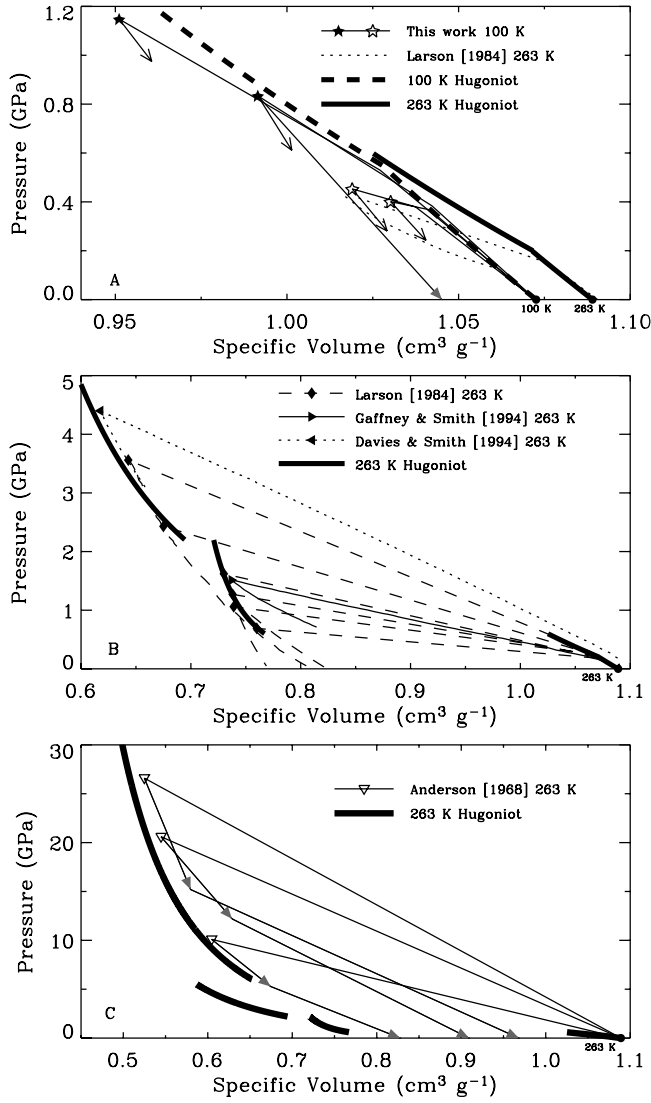


**Figure 15.** Shock loading and release paths shown with ice Hugoniot (thick lines). No error bars shown. (a) Release paths from ice Ih region lie below Hugoniot, indicating residual strength during release. Open star data points are partially released. (b) Release paths from ice VI and VII regions follow Hugoniot, indicating unloading in the high-pressure phase. (c) Release paths from liquid water region lie above Hugoniot, indicating release as pure liquid water.

where  $V$  is specific volume and fluid rheology during release is assumed [cf. *McQueen*, 1991]. The release wave arrives from the sample free surface (geometry A, Figure S1), and the initial slope of the release isentropes are indicated with V-shaped arrowheads at the terminus of the unloading path in Figure 15.

[89] (3) The particle velocity is measured at a known pressure on the release path and the release volume is derived using the Riemann integral [cf. *Ahrens et al.*, 1969] assuming a straight line path in the  $u_p - P$  plane between the volume on the Hugoniot,  $V_H$ , and the volume on the release path,  $V_R$ :

$$V_R = V_H + \int_{u_{p,R}}^{u_{p,H}} \left( \frac{du_p}{dP} \right)_S du_p. \quad (28)$$

These intermediate and final release states are indicated by solid gray arrowheads in Figure 15 [*Anderson*, 1968; this work]. Note that the volume derived from this method, when the unloading path is approximated via a straight line in the  $P$ - $V$  plane, provides only a lower bound to the true volume in the fully unloaded state [*Lyzenga and Ahrens*, 1978]. However, the inferred volume can be useful for deriving the trend in the release path (below, along, or above the Hugoniot).

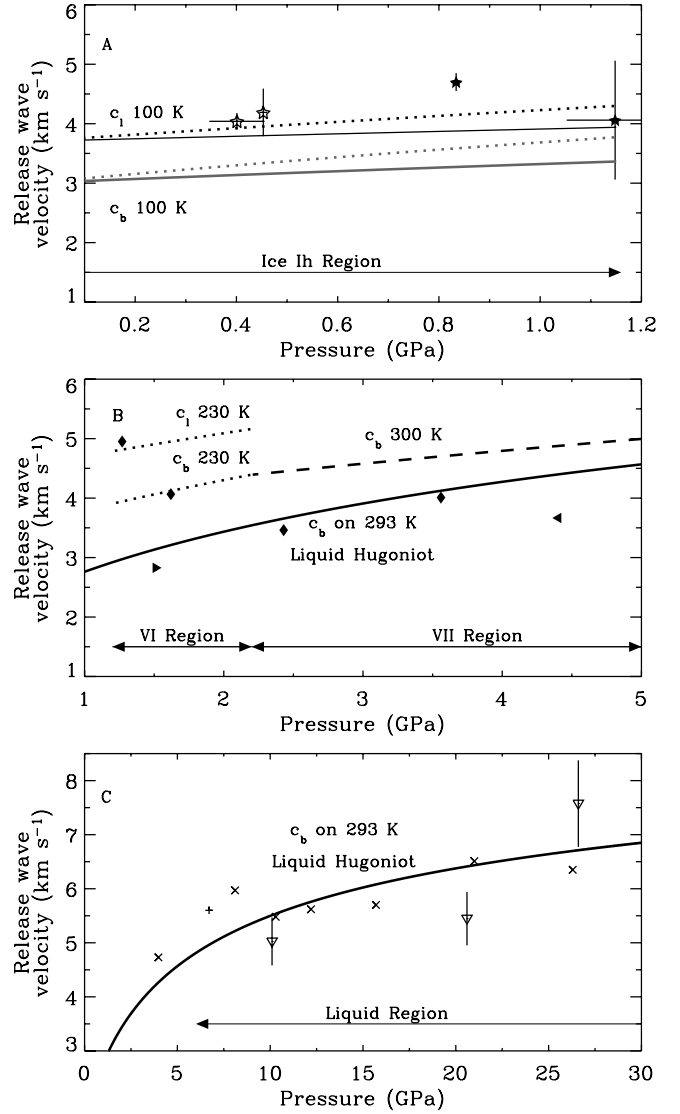


**Figure 16.** Release wave velocities versus pressure on ice Hugoniot. (a) Release velocity data with ice Ih longitudinal ( $c_l$ , black lines) and bulk ( $c_b$ , gray lines) sound velocities for  $dK_T/dP = 3.0$  (Table 4), solid lines, and  $dK_T/dP = 5.5$  [*Shaw*, 1986], dotted lines. Open star data points are partially released. (b) Release velocity data and sound velocities in ice VI [*Gagnon et al.*, 1990; *Shaw*, 1986; *Tulk et al.*, 1997], ice VII [*Fei et al.*, 1993], and along the liquid water Hugoniot. No error bars shown. (c) Release wave velocity data in liquid region on ice Hugoniot ( $\nabla$ ) [*Anderson*, 1968] with calculated sound speed (solid line, see text) and release velocity data (+ [*Al'tshuler et al.*, 1960] and  $\times$  [*Bakanova et al.*, 1976]) along 293 K liquid water Hugoniot.

[90] The measured or derived sound velocities on the Hugoniot are given in Figure 16. The sound velocity in the ice Ih region is compared to the longitudinal ( $c_l$ ) and bulk ( $c_b$ ) sound speeds along 100 K isotherms in Figure 16a. The  $T_0 = 100$  K release wave arrivals are very close to those expected for a longitudinal wave velocity [Shaw, 1986]; hence shocked ice retains strength along the Hugoniot, up to the ice Ih shock cusp at 1.16 GPa when the sound speed drops. We do not show the release wave profile published by Larson [1984] because a steady shock wave did not develop in that experiment with a peak shock pressure of about 0.5 GPa.

[91] In the ice VI and VII regions of the 263 K Hugoniot (Figure 16b), the velocities of release waves propagating through the mixed solid-liquid regions are highly scattered. Larson data at 1.3 and 1.6 GPa indicates release at longitudinal and bulk velocities in the ice VI region, whereas Gaffney and Smith's datum and Larson's data in the ice VII region lie well below  $c_b$ , near the values for pure water. The  $T_0 = 263$  K data should be a mixture of liquid and ice VI or ice VII, reducing the sound speeds below the  $c_b$  of ice VI and VII.

[92] The release paths in the ice VI and VII regions (Figure 15) are consistent with the mixed phase, constant mass fraction of phases release model. In this model, the mixed phases in the shocked material remain a constant mixture assemblage over most of the release path, reverting to equilibrium phases near ambient pressure [cf. Sekine *et al.*, 1995]. Notably, Larson [1984] reports release paths from 0.6 to 3.56 GPa to zero pressure which are consistent with initial unloading of a high-pressure phase.

[93] Above 6 GPa, liquid water forms on the ice Hugoniot, and the release paths, which lie above the Hugoniot, are consistent with release in the liquid state (Figure 16c). The inferred sound velocity data agree well with measurements of the sound velocity along the liquid water Hugoniot [Bakanova *et al.*, 1976; Al'tshuler *et al.*, 1960] and the sound speed derived from the water Hugoniot. The sound speed on the water Hugoniot is given by equation (27), where

$$\left(\frac{dP}{dV}\right)_s = \left[1 - \frac{\gamma}{V} \frac{V_0 - V}{2}\right] \frac{dP_H}{dV} + \frac{\gamma}{V} \frac{P_0 - P_H}{2}, \quad (29)$$

$P_H$  and  $V$  are the pressure and volume along the Hugoniot (equation (18)), and  $\gamma$  is the liquid water Mie-Grüneisen parameter (equation (19)) (equation (29) is corrected equation (2.73) from McQueen [1991]).

## 4. Discussion

### 4.1. Impact-Induced Melting on Icy Planetary Surfaces

[94] Unlike anhydrous silicates, where shock-induced melting occurs upon release from shock pressures of 10's–100's GPa [cf. Ahrens and O'Keefe, 1972; Pierazzo *et al.*, 1997], shock-induced melting of ice begins at extremely low pressures, at only a few GPa. Shock-induced melting and metamorphism during impact cratering events are important surface modification processes in the solar system.

[95] New criteria for shock-induced melting of ice are derived from the present shock data and the entropy of

melting under ambient pressure (revised from Stewart and Ahrens [2003]). The release paths and velocities indicate that ice unloads approximately isentropically after shock compression. Thus the shock pressure required for melting upon release may be determined from examination of the Hugoniot in the  $P - S$  phase diagram (Figure 11). The revised shock pressures required to induce incipient melting upon release are  $0.6 \pm 0.05$  and  $1.6 \pm 0.3$  GPa on the 263 and 100 K ice Hugoniot, respectively. The shock pressures required for complete melting upon release are  $2.5 \pm 0.1$  and  $4.1 \pm 0.3$  GPa, respectively.

[96] Previous estimates of the critical pressures for melting have been 2–10 times higher. Kieffer and Simonds [1980] derived critical values of 3 GPa for incipient melting and 10 GPa for complete melting under terrestrial conditions, on the basis of sparse H<sub>2</sub>O shock data. Ahrens and O'Keefe [1985] report 7.6 and 10.8 GPa for IM and CM, respectively, at 70 K and 1 bar, and 6.2 and 9.6 GPa, at 263 K and 1 bar. The theoretical estimates at 263 K [Pierazzo *et al.*, 1997], derived from a simplified equation of state that does not include solid-solid phase transformations, are consistent with the 263 K critical pressures we report here.

[97] The new criteria for shock-induced melting of water ice have broad application in the solar system. Widespread melting during impact crater formation will soften crater morphologies [Turtle and Pierazzo, 2001] and incorporate liquid water into ejecta blankets [Stewart, 2002]. Stewart *et al.* [2001, 2004] conducted simulations of impact cratering onto ice-silicate mixtures that demonstrate fluidization of ejecta blankets, related to distal scarp structures called ramparts. Rampart crater morphologies, found in great abundance on Mars [Carr *et al.*, 1977], are also seen on the icy surfaces of Europa [Moore *et al.*, 1998; Turtle and Pierazzo, 2001] and Ganymede [Horner and Greeley, 1982]. The new H<sub>2</sub>O Hugoniot shows that the pressures required for shock-induced melting during impact cratering upon the cold icy satellites of the outer solar system are even lower than previously assumed.

[98] These results also have implications for collisional processing of comets before ejection into the Oort cloud [Stern and Weissman, 2001] (mutual impact velocities of 100's m s<sup>-1</sup>) and within the Kuiper belt [Dorda and Stern, 2000] (present mutual collisions at ~1000 m s<sup>-1</sup>). Although collisions between pure ice at crystal density would not suffer shock-induced melting at these velocities, cometary objects, expected to be mixtures of ice, organic, and silicate materials with 30–80% porosity will readily undergo partial melting. We conclude that shock-induced melting of ice should be widespread in planetary impact processes and mutual collisions between icy comets.

### 4.2. Formation of Metastable High-Pressure Ice Polymorphs From Impact Events

[99] Our analysis of the solid ice Hugoniot motivates a critical re-examination of the hypothesis by Gaffney and Matson [1980] that high-pressure ice polymorphs created by shock-processes may remain metastable upon release. The 100 K Hugoniot is an appropriate reference for shock-induced phase changes from impact events in the icy outer solar system. We have shown that shocks to pressures below about 1 GPa along the 100 K Hugoniot are approximately isentropic and the temperature increase from the shock is

small (10's K, Figure 9). Hence ice VI may remain metastable after a shock under conditions limited to initial temperatures  $\leq 100$  K and shock pressures of about 1 GPa. Shock-induced formation of ice VI will not occur in great abundance during hypervelocity impacts upon icy planetary surfaces. It is plausible that nonporous ice in the cold outer solar system, subject to shocks with amplitudes just above 1 GPa may form ice VI, which could remain metastable upon release. Ice II is probably not formed during impact events because the amplitude of ice Ih deformation shocks exceed the ice II stability field (Figure 7).

[100] For shocks above 2 GPa, on the other hand, the increase in entropy, and corresponding increase in temperature, is probably too large for ice VII to be recovered under ambient conditions. Under shocks greater than about 4 GPa, ice will completely melt upon release and slowly freeze and sublimate from conductive and radiative processes.

[101] At the lowest temperatures in the outer solar system, e.g., at Pluto and the Kuiper Belt, other phases of ice may be important in shock processes, e.g., the amorphous phases. These should be examined in future studies with temperatures below 100 K. We note that the increase in entropy from shock compression of porous ice will be larger than solid ice because of the larger initial volume.

## 5. Conclusions

[102] 1. We have conducted an experimental investigation of the H<sub>2</sub>O ice Hugoniot at initial temperatures of 100 K, for application to the outer solar system. Analysis of the combined data, from this study and previous work at 263 K, shows that shock-induced phase transformations to ice VI and VII are the dominant features along the Hugoniot at pressures below 6 GPa, which results in the generation of multiple-wave shock fronts. Along the 100 and 263 K Hugoniots, the shock state is a mixture of solid and liquid at 5.5 and 0.6 GPa and fully liquid at pressures above 9.1 and 6.7 GPa, respectively.

[103] 2. We have identified five regions on the ice Hugoniot: (1) elastic shocks, (2) ice Ih deformation shocks, transformation shocks to (3) ice VI, (4) ice VII, and (5) liquid water. In each region, data obtained at different initial temperatures are described by a single  $U_S - \Delta u_p$  shock equation of state. Use of  $\Delta u_p$  explicitly accounts for the temperature-dependent response of elastic and ice Ih deformation shocks.

[104] 3. The dynamic strength of ice Ih is strongly dependent on temperature. The Hugoniot Elastic Limit varies from 0.05 to 0.62 GPa, as a function of both temperature and peak shock stress.

[105] 4. Ice Ih deformation shocks do not propagate as steady shock waves except at low temperatures as an intermediate shock wave in a three-wave shock front, consisting of the elastic precursor, ice Ih deformation shock, and transformation shock to ice VI. Under temperate conditions, or when subject to peak stress less than 0.6 GPa, the ice Ih shock decays as it propagates. Along the ice Ih region of the Hugoniot, a cusp at 1.16 GPa defines the maximum stress attainable by an ice Ih deformation shock.

[106] 5. We calculate the temperature and entropy along the 100 and 263 K Hugoniots and derive the critical pressures for shock-induced incipient (IM) and complete

(CM) melting upon release. At 100 K, the critical pressures are about 1.6 and 4.1 GPa for IM and CM, respectively. At 263 K, the critical pressures, 0.6 and 2.5 GPa for IM and CM, are 2–10 times lower than inferred in previous work.

[107] 6. Shock-induced ice VI may remain metastable upon release from shock pressures of about 1 GPa and below about 100 K, where the low ambient temperatures inhibit the reverse transformation to ice Ih. The increase in entropy and temperature upon shock transformation to ice VII prevents recovery of the high-pressure phase upon release. Thus shock-induced formation of high-pressure solid ice polymorphs should be relatively rare. Shock-induced melting of ice, however, will be widespread in impact events.

[108] **Acknowledgments.** This work was supported by the Planetary Geology and Geophysics program under NASA Goddard grant NAG5-10198. We appreciate technical support from M. Long, E. Gelle, and C. McCaughey and thank B. Kamb for use of the Caltech cold laboratory. We are grateful to two anonymous reviewers and Francis Nimmo for their useful comments. Contribution 8946, Division of Geological and Planetary Sciences, California Institute of Technology.

## References

- Ahrens, T. J. (1987), Shock wave techniques for geophysics and planetary physics, in *Geophysics*, vol. 24A, *Methods of Experimental Physics*, edited by C. Sammis and T. Henyey, chap. 6, pp. 185–235, Elsevier, New York.
- Ahrens, T. J., and J. D. O'Keefe (1972), Shock melting and vaporization of lunar rocks and minerals, *Moon*, 4, 214–249.
- Ahrens, T. J., and J. D. O'Keefe (1985), Shock vaporization and the accretion of the icy satellites of Jupiter and Saturn, in *Ices in the Solar System*, edited by J. Klinger et al., pp. 631–654, Springer, New York.
- Ahrens, T. J., and M. H. Ruderman (1966), Immersed-foil method for measuring shock wave profiles in solids, *J. Appl. Phys.*, 37(13), 4758–4765.
- Ahrens, T. J., C. F. Peterson, and J. T. Rosenberg (1969), Shock compression of feldspars, *J. Geophys. Res.*, 74(10), 2727–2746.
- Al'tshuler, L. V., S. B. Kormer, M. I. Brazhnik, L. A. Vladimirov, M. P. Speranskaya, and A. I. Funtikov (1960), The isentropic compressibility of aluminum, copper, lead, and iron at high pressures, *Sov. Phys. JETP, Engl. Transl.*, 11(4), 766–775.
- Anderson, G. D. (1968), The equation of state of ice and composite frozen soil material, *Res. Rep. 257*, Cold Regions Res. and Eng. Lab., Hanover, N. H.
- Arakawa, M., K. Shirai, and M. Kato (2000), Shock wave and fracture propagation in water ice by high velocity impact, *Geophys. Res. Lett.*, 27(3), 305–308.
- Bakanova, A. A., V. N. Zubarev, Y. N. Sutulov, and R. F. Trunin (1976), Thermodynamic properties of water at high pressures and temperatures, *Sov. Phys. JETP, Engl. Transl.*, 41(3), 544–548.
- Bancroft, D., E. L. Peterson, and S. Minshall (1956), Polymorphism of iron at high pressure, *J. Appl. Phys.*, 27(1), 291–298.
- Bevington, P. R., and D. K. Robinson (1992), *Data Reduction and Error Analysis for the Physical Sciences*, 2nd ed., McGraw-Hill, New York.
- Carr, M. H., L. S. Crumpler, J. A. Cutts, R. Greeley, J. E. Guest, and H. Masursky (1977), Martian impact craters and emplacement of the ejecta by surface flow, *J. Geophys. Res.*, 82(28), 4055–4065.
- Cowperthwaite, M., and R. F. Williams (1971), Determination of constitutive relationships with multiple gauges in nondivergent waves, *J. Appl. Phys.*, 42(1), 456–462.
- Davies, F. W., and E. A. Smith (1994), High pressure equation of state investigation of rocks, *Tech. Rep. DNA-TR-94-1*, Def. Nucl. Agency, Ktech Corp., Albuquerque, N. M.
- Dolan, D. H. (2003), Time dependent freezing of water under multiple shock wave compression, Ph.D. thesis, Washington State Univ., Pullman.
- Dorsey, N. E. (Ed.) (1940), *Properties of Ordinary Water-Substance*, Reinhold, New York.
- Dremin, A. N., and G. A. Adadurov (1964), The behavior of glass under dynamic loading, *Sov. Phys. Solid State*, 6(6), 1379–1384.
- Dremin, A. N., and K. K. Shvedov (1964), Estimation of Chapman-Jouget pressure and time of reaction in detonation waves of powerful explosives, *J. Appl. Mech. Tech. Phys.*, 2, 154–159.
- Durda, D. D., and S. A. Stern (2000), Collision rates in the present-day Kuiper Belt and Centaur regions: Applications to surface activation and



- modification on comets, Kuiper Belt objects, Centaurs, and Pluto-Charon, *Icarus*, 145, 220–229, doi:10.1006/icar.1999.6333.
- Durham, W., and L. Stern (2001), Rheological properties of water ice—Applications to satellites of the outer planets, *Annu. Rev. Earth Planet. Sci.*, 29, 295–330, doi:10.1146/annurev.earth.29.1.295.
- Durham, W., H. Heard, and S. Kirby (1983), Experimental deformation of polycrystalline H<sub>2</sub>O ice at high-pressure and low-temperature: Preliminary results, *J. Geophys. Res.*, 88, B377–B392.
- Durham, W., S. Kirby, and L. Stern (1998), Rheology of planetary ices, in *Solar System Ices*, edited by B. Schmitt, C. de Bergh, and M. Festou, pp. 63–78, Springer, New York.
- Fei, Y., H.-K. Mao, and R. J. Hemley (1993), Thermal expansivity, bulk modulus, and melting curve of H<sub>2</sub>O-ice VII to 20 GPa, *J. Chem. Phys.*, 99(7), 5369–5373.
- Fowles, R. (1967), Dynamic compression of quartz, *J. Geophys. Res.*, 72(22), 5729–5742.
- Fowles, R., and R. F. Williams (1970), Plane stress wave propagation in solids, *J. Appl. Phys.*, 41(1), 360–363.
- Frank, M. R., Y. W. Fei, and J. Z. Hu (2004), Constraining the equation of state of fluid H<sub>2</sub>O to 80 GPa using the melting curve, bulk modulus, and thermal expansivity of Ice VII, *Geochim. Cosmochim. Acta*, 68(13), 2781–2790, doi:10.1016/j.gca.2003.12.007.
- Gaffney, E. S. (1973), Study of the nature of shock waves in frozen earth materials, *Rep. SSS-R-73-1557*, Syst. Sci. and Software, La Jolla, Calif.
- Gaffney, E. S. (1985), Hugoniot of water ice, in *Ices in the Solar System*, edited by J. Klinger et al., pp. 119–148, Springer, New York.
- Gaffney, E. S., and T. J. Ahrens (1980), Identification of ice VI on the Hugoniot of ice Ih, *Geophys. Res. Lett.*, 7(6), 407–409.
- Gaffney, E. S., and D. L. Matson (1980), Water ice polymorphs and their significance on planetary surfaces, *Icarus*, 44, 511–519.
- Gaffney, E. S., and E. A. Smith (1994), HYDROPLUS experimental study of dry, saturated, and frozen geological materials, *Tech. Rep. DNA-TR-93-74*, Def. Nucl. Agency, Ktech Corp., Albuquerque, N. M.
- Gagnon, R., H. Kieffe, M. Clouter, and E. Whalley (1988), Pressure dependence of the elastic constants of ice Ih to 2.8 kbar by Brillouin spectroscopy, *J. Chem. Phys.*, 89(8), 4522–4528.
- Gagnon, R. E., H. Kieffe, and M. J. Clouter (1990), Acoustic velocities and densities of polycrystalline ice Ih, II, III, V, and VI by Brillouin spectroscopy, *J. Chem. Phys.*, 92(3), 1909–1914.
- Giauque, W. F., and J. W. Stout (1936), The entropy of water and the third law of thermodynamics, *J. Am. Chem. Soc.*, 58, 1144–1150.
- Haida, O., T. Matsuo, H. Suga, and S. Seki (1974), Calorimetric study of the glassy state X: Enthalpy relaxation at the glass-transition temperature of hexagonal ice, *J. Chem. Thermodyn.*, 6(9), 815–825.
- Hawkes, I., and M. Mellor (1972), Deformation and fracture of ice under uniaxial stress, *J. Glaciol.*, 11(61), 103–131.
- Hobbs, P. V. (1974), *Ice Physics*, Clarendon, Oxford, U. K.
- Horner, V. M., and R. Greeley (1982), Pedestal craters on Ganymede, *Icarus*, 51, 549–562.
- Jeanloz, R. (1979), Properties of iron at high pressures and the state of the core, *J. Geophys. Res.*, 84(B11), 6059–6069.
- Jeanloz, R. (1989), Shock wave equation of state and finite strain theory, *J. Geophys. Res.*, 94(B5), 5873–5886.
- Kato, M., M. Higa, K. Shirai, Y. Iijima, T. Kiyono, S. Nakazawa, and M. Arakawa (2001), Shock pressure attenuation in water ice at a pressure below 1 GPa, *J. Geophys. Res.*, 106, 17,567–17,578.
- Kieffer, S. W., and C. H. Simonds (1980), The role of volatiles and lithology in the impact cratering process, *Rev. Geophys.*, 18(1), 143–181.
- Korner, S. B. (1968), Optical study of the characteristics of shock-compressed condensed dielectrics, *Sov. Phys. Usp., Engl. Transl.*, 11(2), 229–254.
- Lange, M. A., and T. J. Ahrens (1983), The dynamic tensile strength of ice and ice-silicate mixtures, *J. Geophys. Res.*, 88, 1197–1208.
- Larson, D. (1984), Shock-wave studies of ice under uniaxial strain conditions, *J. Glaciol.*, 30(105), 235–240.
- Larson, D. B., G. D. Bearson, and J. R. Taylor (1973), Shock-wave studies of ice and two frozen soils, in *Permafrost: The North American Contribution to the Second International Conference*, pp. 318–325, Natl. Acad. of Sci., Washington, D. C.
- Lawton, H., and I. C. Skidmore (1955), Hugoniot curves for inert solids and condensed explosives, *Disc. Faraday Soc.*, 22, 188–195.
- Loree, T. R., F. S. Minshall, and D. Stirpe (1965), The overdriving effect in dynamic polymorphism, *Tech. Rep. LA-3215*, Los Alamos Lab., Los Alamos, N. M.
- Lyzenga, G. A., and T. J. Ahrens (1978), Relation between shock-induced free-surface velocity and post-shock specific volume of solids, *J. Appl. Phys.*, 49(1), 201–204.
- Lyzenga, G. A., T. J. Ahrens, W. J. Nellis, and A. C. Mitchell (1982), The temperature of shock-compressed water, *J. Chem. Phys.*, 76(12), 6282–6286.
- Marsh, S. P. (Ed.) (1980), *LASL Shock Hugoniot Data*, Univ. of Calif. Press, Berkeley.
- Mashimo, T., M. Uchino, A. Nakamura, T. Kobayashi, E. Takasawa, T. Sekine, Y. Noguchi, H. Hikosaka, K. Fukuoka, and Y. Syono (1999), Yield properties, phase transition, and equation of state of aluminum nitride (AlN) under shock compression up to 150 GPa, *J. Appl. Phys.*, 86(12), 6710–6716.
- McQueen, R. G. (1991), Shock waves in condensed media: their properties and the equation of state of materials derived from them, in *High-Pressure Equations of State: Theory and Applications*, pp. 101–216, Elsevier, New York.
- Meyers, M. A. (1994), *Dynamic Behavior of Materials*, John Wiley, Hoboken, N. J.
- Miller, G., E. Stolper, and T. Ahrens (1991), The equation of state of a molten Komatiite: 1. Shock-wave compression to 36 GPa, *J. Geophys. Res.*, 96(B7), 11,831–11,848.
- Minshall, S. (1955), Investigation of a polymorphic transition in iron at 130 k.b., *Phys. Rev.*, 98(1), 271.
- Mishima, O., N. Mori, and S. Endo (1979), Thermal expansion anomaly of ice VI related to the order-disorder transition, *J. Chem. Phys.*, 70(4), 2037–2038.
- Mitchell, A. C., and W. J. Nellis (1982), Equation of state and electrical conductivity of water and ammonia shocked to the 100 GPa (1 Mbar) pressure range, *J. Chem. Phys.*, 76(12), 6273–6281.
- Moore, J., et al. (1998), Large impact features on Europa: Results of the Galileo nominal mission, *Icarus*, 135(1), 127–145.
- Murnaghan, F. D. (1944), The compressibility of media under extreme pressure, *Proc. Natl. Acad. Sci. U. S. A.*, 30, 244–247.
- Nagayama, K., Y. Mori, K. Shimada, and M. Nakahara (2002), Shock Hugoniot compression curve for water up to 1 GPa by using a compressed gas gun, *J. Appl. Phys.*, 91(1), 476–482, doi:10.1063/1.1421630.
- Petersen, C. F., W. J. Murri, and M. Cowperthwaite (1970), Hugoniot and release-adiabat measurements for selected geologic materials, *J. Geophys. Res.*, 75(11), 2063–2072.
- Petrenko, V. F., and R. W. Whitworth (1999), *Physics of Ice*, Oxford Univ. Press, New York.
- Pierazzo, E., A. Vickery, and H. Melosh (1997), A reevaluation of impact melt production, *Icarus*, 127(2), 408–423.
- Rice, M. H., and J. M. Walsh (1957), Equation of state of water to 250 kilobars, *J. Chem. Phys.*, 26(4), 824–830.
- Rice, M. H., R. G. McQueen, and J. M. Walsh (1958), Compression of solids by strong shock waves, *Solid State Phys.*, 6, 1–63.
- Rosenberg, Z., N. Brar, and S. Bless (1991), Dynamic high-pressure properties of AlN ceramic as determined by flyer plate impact, *J. Appl. Phys.*, 70(1), 167–169.
- Röttger, K., A. Endriss, J. Ihringer, S. Doyle, and W. Kuhs (1994), Lattice constants and thermal expansion of H<sub>2</sub>O and D<sub>2</sub>O ice Ih between 10 and 265 K, *Acta Crystallogr., Sect. B Struct. Sci.*, B50(6), 644–648.
- Ruoff, A. L. (1967), Linear shock-velocity-particle-velocity relationship, *J. Appl. Phys.*, 38(13), 4976–4980.
- Sekine, T., T. Duffy, A. Rubin, W. Anderson, and T. Ahrens (1995), Shock compression and isentropic release of granite, *Geophys. J. Int.*, 120(2), 247–261.
- Sharipdzhanov, I. I., L. V. Al'tshuler, and S. E. Brusnikin (1984), Anomalies in the shock and isentropic compressibilities of water, *Combust. Explos. Shock Waves*, 19(5), 668–672.
- Shaw, G. H. (1986), Elastic properties and equation of state of high pressure ice, *J. Chem. Phys.*, 84(10), 5862–5868.
- Simmons, G., and H. Wang (1971), *Single Crystal Elastic Constants and Calculated Aggregate Properties: A Handbook*, MIT Press, Cambridge, Mass.
- Skidmore, I. C., and E. Morris (1962), Experimental equation of state data for uranium and its interpretation in the critical region, in *Thermodynamics of Nuclear Materials*, pp. 173–216, Int. At. Energy Agency, Vienna.
- Snay, H. G., and J. H. Rosenbaum (1952), Shockwave parameters in fresh water for pressures up to 95 kilobars, *NAVORD Rep. 2383*, U.S. Nav. Ordnance Lab., White Oak, Md.
- Sotin, C., O. Grasset, and S. Beauchesne (1998), Thermodynamic properties of high pressure ices: Implications for the dynamics and internal structure of large icy satellites, in *Solar System Ices*, edited by B. Schmitt, C. de Bergh, and M. Festou, pp. 79–96, Springer, New York.
- Stern, S., and P. Weissman (2001), Rapid collisional evolution of comets during the formation of the Oort cloud, *Nature*, 409, 589–591, doi:10.1038/35054508.
- Stewart, S. T. (2002), Collisional processes involving icy bodies in the solar system, Ph.D. thesis, Calif. Inst. of Technol., Pasadena.
- Stewart, S. T., and T. J. Ahrens (1999), Correction to the dynamic tensile strength of ice and ice-silicate mixtures (Lange & Ahrens 1983), *Proc. Lunar Planet. Sci. Conf.*, 30th, abstract 2037.

- Stewart, S. T., and T. J. Ahrens (2003), Shock Hugoniot of H<sub>2</sub>O ice, *Geophys. Res. Lett.*, **30**(6), 1332, doi:10.1029/2002GL016789.
- Stewart, S., J. O’Keefe, and T. Ahrens (2001), The relationship between rampart crater morphologies and the amount of subsurface ice, *Proc. Lunar Planet. Sci. Conf.*, **32nd**, abstract 2092.
- Stewart, S., T. Ahrens, and J. O’Keefe (2004), Impact-induced melting of near-surface water ice on Mars, in *Shock Compression of Condensed Matter—2003*, edited by M. D. Furnish, Y. M. Gupta, and J. W. Forbes, pp. 1484–1487, AIP, New York.
- Swegle, J. W., and D. E. Grady (1985), Shock viscosity and the prediction of shock wave rise times, *J. Appl. Phys.*, **58**(2), 692–701.
- Tulk, C., H. Kieft, M. Clouter, and R. Gagnon (1997), Elastic constants of ice III, V, and VI by Brillouin spectroscopy, *J. Phys. Chem. B*, **101**, 6154–6157, doi:10.1021/jp963183d.
- Turtle, E. P., and E. Pierazzo (2001), Thickness of a European ice shell from impact crater simulations, *Science*, **294**, 1326–1328, doi:10.1126/science.1062492.
- Voigt, W. (1928), *Lehrbuch der Krystallphysik*, B. G. Teubner, Leipzig, Germany.
- Volkov, L. P., N. P. Voloshin, R. A. Mangasarov, V. A. Simonenko, G. V. Sinko, and V. L. Sorokin (1980), Shock compressibility of water under pressure  $\sim 1$  Mbar, *JETP Lett.*, **31**(9), 546–548.
- Wagner, W., and A. Pruss (2002), The IAPWS formulation 1995 for the thermodynamic properties of ordinary water substance for general and scientific use, *J. Phys. Chem. Ref. Data*, **31**(2), 387–535, doi:10.1063/1.1461829.
- Woolfolk, R. W., M. Cowperthwaite, and R. Shaw (1973), A “universal” Hugoniot for liquids, *Thermochim. Acta*, **5**, 409–414.
- Zel’dovich, Y., and Y. Raizer (2002), *Physics of Shock Waves and High-Temperature Hydrodynamic Phenomena*, Dover, Mineola, N. Y.
- 
- T. J. Ahrens, Division of Geological and Planetary Sciences, California Institute of Technology, MC 252-21, Pasadena, CA 91125, USA. (tja@gps.caltech.edu)
- S. T. Stewart, Department of Earth and Planetary Sciences, Harvard University, 20 Oxford Street, Cambridge, MA 02138, USA. (sstewart@eps.harvard.edu)